# From droplets to waves:

# Periodic instability patterns in highly viscous microfluidic flows

Xiaoyi Hu and Thomas Cubaud<sup>1</sup>

Department of Mechanical Engineering, Stony Brook University, Stony Brook, New York 11794 USA

### **ABSTRACT**

We experimentally study the transition from droplet to wave regimes in microfluidic liquid/liquid multiphase flows having large differences in viscosity. A unified approach based on periodic pattern analysis is employed to study relationships between dispersed and separated flow regimes, including dripping, jetting, capillary waves, inertial waves, and core-annular flows over a wide range of flow rates and viscosity contrasts. We examine the morphology and dynamics of each flow regime based on wavelength, frequency, and velocity of repeating unit cells to elucidate their connections and develop predictive capabilities based on dimensionless control parameters. We demonstrate in particular that pattern selection is contingent upon propagation velocity of droplets and waves at the transition. We also investigate microfluidic wave breaking phenomena with the formation of ligaments and droplets from wave crests in both capillary and inertial wave regimes. This work expands conventional multiphase flow regimes observed in microchannels and shows new routes to disperse highly viscous materials using interfacial waves dynamics in confined microsystems.

<sup>&</sup>lt;sup>1</sup> Author to whom correspondence should be addressed. Email address: thomas.cubaud@stonybrook.edu

#### 1. Introduction

Flow regime prediction of multiphase flows in confined geometries is important for many engineering techniques and industrial processes and remains a challenging problem in fundamental fluid mechanics (Brennen 2005; Crowe 2006; Cheng, Ribatski & Thome 2008). Flow patterns can indeed adopt various interfacial morphologies and dynamics, leading to diverse mechanisms for the transport of mass, momentum, and energy (Bird, Stewart & Lightfoot 2002). While the motion of a single-phase flow depends on the interplay between inertial and viscous forces, the behavior of two-phase flows involves numerous parameters, including bulk fluid properties, such as densities and viscosities, and interfacial properties, such as surface tension. In addition, flow destabilization processes also depend on flow parameters and local geometries, including Plateau-Rayleigh instabilities, where liquid threads break into droplets due to interfacial tension, Kelvin-Helmholtz instabilities between streams having large differences in velocities, Rayleigh-Taylor instabilities for heavier fluids setting on top of lighter ones, and Saffman-Taylor instabilities when a less viscous fluid is injected through a thick fluid in confined geometries (Drazin & Reid 2004). In general, hydrodynamic stability analysis of open flows includes (a) convective instabilities, where flow perturbations are advected downstream, and (b) absolute instabilities, where perturbations can also propagate upstream (Huerre & Rossi 2005; Salin & Talon 2019). Linear stability analysis of base flow provides a useful framework for determining regions of stability and flow characteristics, however, less is known about the evolution of fluid morphologies and pattern dynamics at the transition between flow regimes.

Due to considerable industrial interests, liquid-gas flows have been significantly studied in channels of various sizes and a wide range of flow patterns have been classified, such as bubbly, slug, churn, stratified, wavy, mist, and core-annular flows (Triplett, *et al.* 1999; Cubaud, Ulmanella & Ho 2006; Berna, *et al.* 2015). Multiphase flow patterns can also be grouped into two categories, including (a) dispersed flows, where one phase forms discrete elements in the other continuous phase, and (b) separated flows, where both phases form continuous streams (Crowe 2006). A difficulty in predicting regime selection of dispersed and separated flows lays in the different methods used to analyze each flow pattern and a unifying approach would improve predictive knowledge of multiphase flows.

Microfluidic technologies provide advanced experimental platforms with fine control over flow rates and microgeometries to investigate the role of fluid properties on multiphase flow instabilities (Hu & Cubaud 2018). For liquid-liquid systems, monodisperse droplet dispersions can be steadily generated using microchannels and find use to encapsulate reagents in domains such diverse as material synthesis, drug discovery and food industry (Barrero & Loscertales 2007; Baroud, Gallaire & Dangla 2010; Anna 2016; Evangelio, Campos-Cortés & Gordillo 2016; Mowlavi, *et al.* 2019). Two common regimes of droplet formation have been identified as dripping and jetting based on the location of droplet pinch-off from the fluid junction (Eggers 1997; Guillot, *et al.* 2007; Cubaud & Mason 2008; Nunes, *et al.* 2013; Gordillo, Sevilla & Campo-Cortés 2014). The regime transition between dripping droplets, which form in the upstream region near the fluid contactor, and jetting droplets generated from

a slender thread further downstream corresponds to a shift from an absolute and a convective instability of dispersed flows (Utada, *et al.* 2008; Augello, Fani & Gallaire 2018). Linear stability analysis shows good agreement with data for delineating the absolute/convective instability transition between dripping droplets and jets in coaxial flows (Guillot, *et al.* 2007).

In the context of separated flows, the hydrodynamic stability of viscous stratifications has been theoretically and numerically investigated (Yih 1967; Hinch 1984; Selvam, et al. 2007; Govindarajan & Sahu 2014) and the development of interfacial waves in viscous-stratified flows was experimentally reported in various configurations (Sangalli, et al. 1995; Al-Wahaibi & Angeli 2011; Hu & Cubaud 2016). When an inner stream is unsheathed with another fluid, the destabilization of miscible and immiscible core-annular flows has been studied in small tubes with the appearance of interfacial waves (Cao, et al. 2003), including bamboo waves (Joseph & Renardy 1993) and pearl-mushroom waves (d'Olce, et al. 2008), which result from the development of absolute instabilities (Salin & Talon 2019). In microchannels, a variety of instability patterns were examined based on fluid and flow properties during the formation of miscible viscous threads (Cubaud & Notaro 2014). Overall, the development of periodic flow patterns allows for relating flow characteristics to control parameters and provides insight into hydrodynamic instabilities. A general approach, however, is needed to clarify regime transitions and relationships between dispersed and separated flows in connection with convective and absolute instabilities.

In this article, we examine the microflow behaviour of immiscible fluids having large difference in viscosity using square focusing sections. A variety of dispersed and separated flows are systematically characterized using a single microflow geometry to compare regimes and determine transitions. In particular, a periodic pattern description is employed to relate wavelength, frequency, and celerity of repeating unit cells within each flow pattern based on control parameters. We proceed with the study of dispersed flows and investigate the relationships between dripping and jetting regimes. We then examine separated flows and discuss the development of capillary and inertial waves along core-annular flows. For a given fluid pair, a rich collection of hydrodynamic phenomena is observed from droplet to wave flow regimes. Our analysis shows that the interfacial velocity of base coreannular flow provides a useful reference to compare patterns across flow regimes. We quantify the transition between regimes using dimensionless numbers and demonstrate that both droplet velocity and wave celerity reach a maximum value at the dispersed/separated flow transition. This insight allows us to develop predictive capabilities for the flow transition in good agreement with experimental data over a wide range of viscosity contrasts.

#### 2. Experimental methods

We employ a microfluidic hydrodynamic focusing section that consists of two square microchannels of height  $h = 250 \mu m$  that intersect perpendicularly (figure 1). The microchannel is made of an etched-trough silicon wafer sandwiched between two borosilicate glass plates to allow visualization. Anodic bonding between glass and silicon allows the chip to withstand the large injection pressures associated with the flow of highly viscous liquids in

micro-confined environments. The microfluidic platform is mounted on an inversed microscope equipped with a high-speed camera to capture fast interfacial dynamics and fluids are injected into the device using high-pressure syringe pumps. Droplets and core-annular flows are generated when a fluid L1 of viscosity  $\eta_1$  is introduced in the central channel at flow rate  $Q_1$  and a more viscous fluid L2 having a viscosity  $\eta_2$  is symmetrically injected through side channels at total flow rate  $Q_2$ . In a typical series of experiments, the flow rate of the high-viscosity fluid  $Q_2$  is fixed and the low-viscosity fluid flow rate  $Q_1$  is varied.

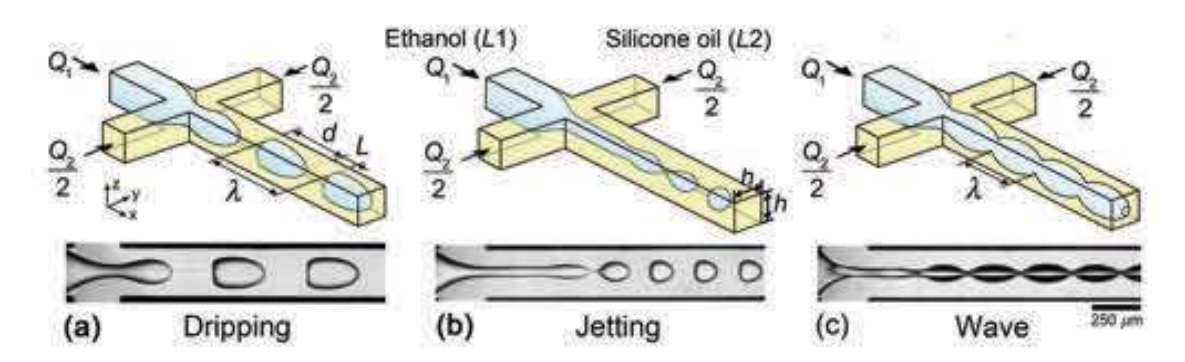


FIGURE 1. (Colour online) Schematics of typical flow patterns with corresponding experimental micrographs. Flow rates in  $\mu$ L/min. (a) Dripping, [( $Q_1$ ,  $Q_2$ ), fluid pair] = [(2, 4), E5h]; (b) jetting, [(2, 20), E50] and (c) wavy [(200, 200), E5h].

Pair	L1	$\eta_1$	$ ho_{ m l}$	L2	$\eta_2$	$ ho_2$	$oldsymbol{\mathcal{X}}^{-1}$	<b>%</b> 12	Symbol
		(cP)	$(g\;mL^{-1})$		(cP)	$(g\;mL^{-l})$		$(mN\ m^{-1})$	
E50	Ethanol	1.07	0.781	Silicone oil	48.5	0.960	45.3	0.65	$\triangle$
E5h					485	0.971	453	1.09	0
E5k					4865	0.977	4547	1.15	$\Diamond$

TABLE 1. Properties of fluids used in experiments, including dynamic viscosity  $\eta$ , viscosity contrast  $\chi^{-1} = \eta_2/\eta_1$ , density  $\rho$ , and interfacial tension  $\eta_2$ .

We systematically examine the microflow of three immiscible fluid pairs having low interfacial tension  $\gamma_{12}$ . The liquid L1 is made of ethanol and L2 consists of silicone oils of various viscosities (Table I). Interfacial tension  $\gamma_{12}$  is measured for each fluid pair using the Du Noüy ring method with a high-precision tensiometer. Data show that  $\gamma_{12}$  remains nearly constant for large variations of the viscosity ratio  $\chi = \eta_1/\eta_2$ , which is typically referred to as viscosity contrast  $\chi^{-1}$  for convenience. Over the range of parameters investigated, the silicone oil L2 is found to wet the channel walls more than ethanol L1, therefore the inner fluid is always lubricated by the viscous outer stream.

Depending on fluid properties and flow rates of injections, a range of microflow arrangements are observed in the outlet channel, including (a) dripping, (b) jetting, and (c) wave regimes (figure 1). In the dripping regime,

droplets are formed near the fluid junction whereas, in the jetting regime, droplets are generated at the tip of a jet further downstream in the channel. Parameters of interest include the average droplet length d, spacing L, and velocity  $V_D$ . The regularity of droplet flows also enables measurement of wavelength  $\lambda = d + L$  of a unit cell. In the wave regimes, periodic undulations of length  $\lambda$  and celerity c develop along the interface formed between the two parallel streams of L1 and L2. In the following, we examine the dynamics of each regime and study pattern transition to better understand the relationship between fluid properties and microfluidic multiphase flows in the presence of large viscosity contrasts.

### 3. Flow regimes and flow maps

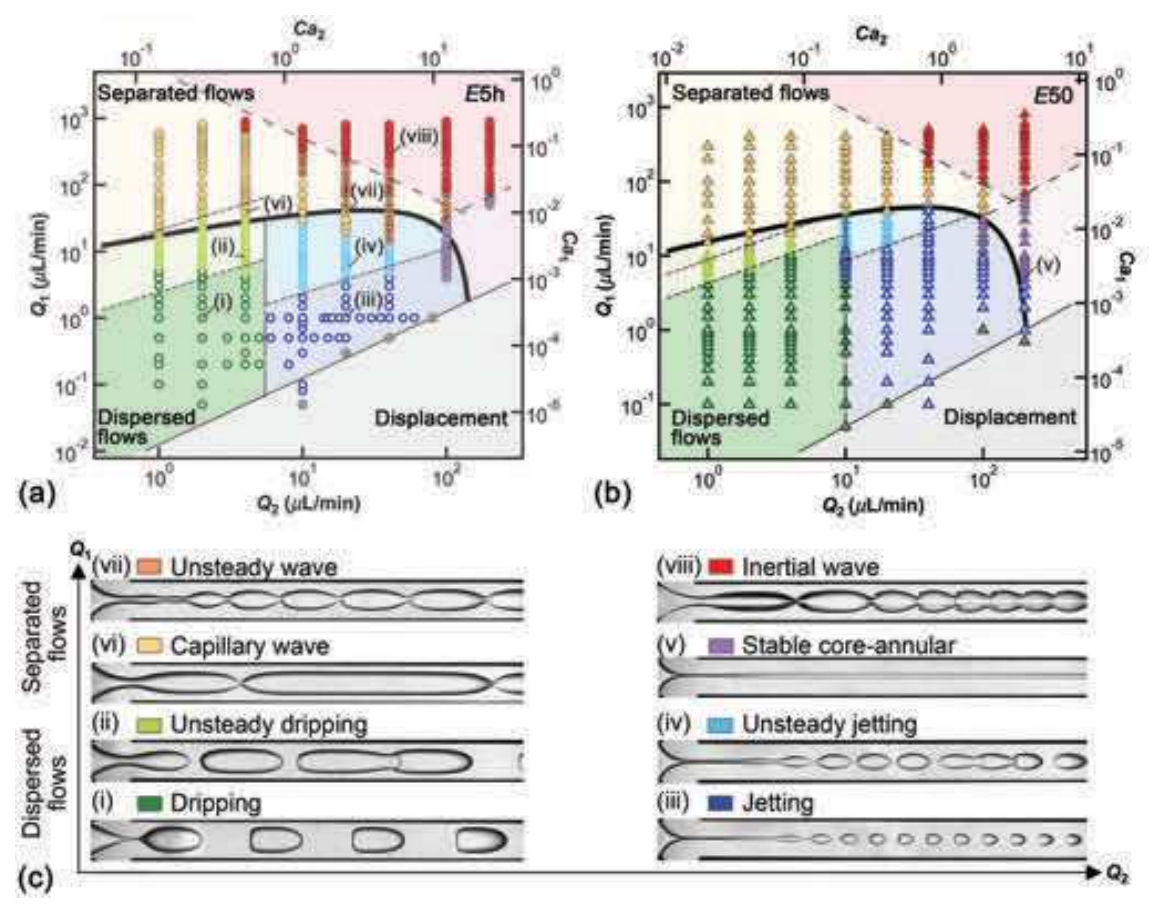


FIGURE 2. (Colour Online) Flow maps of fluid pairs (a) E5h and (b) E50 in terms of flow rates and capillary numbers. See main text for transition curves. (c) Experimental micrographs of flow regimes (Flow rates in  $\mu$ L/min). Dispersed flows: (i) Dripping ( $Q_1$ ,  $Q_2$ ) = (1, 2), (ii) unsteady dripping (9, 4), (iii) jetting (1, 20), and (iv) unsteady jetting (4, 20). Separated flows: (v) stable core-annular (5, 200), (vi) capillary wave (40, 4), (vii) unsteady wave (40, 20), and (viii) inertial wave (350, 40).

Two-phase flow patterns are generally classified as separated flows when both fluids form continuous streams and dispersed flows when a phase forms discrete bubbles or droplets in the other phase. Here, separated flows

correspond to wavy core-annular flows with distinct characteristics while dripping and jetting regimes are treated as dispersed flows. Jetting patterns display intermediate features with the formation of a core-annular flow, or jet, near the junction and the emission of droplets at the tip of the jet in the observation channel. Although separated flow pattern features may further evolve downstream due to the entrainment of filamentous structures from wave crests, we restrict our analysis to relatively short distance  $x/h \sim 16$  from the junction to directly compare initial flow characteristics between all regimes. Analysis of flow behavior near the fluid junction is also relevant for labon-a-chip applications where short microfluidic elements are combined.

For a given fluid pair, variations of both central and side stream flow rates,  $Q_1$  and  $Q_2$ , grant access to a variety of flow regimes as can be seen in figure 2. These quantities are made non-dimensional using capillary numbers such as  $Ca_i = \eta_i J_i / \gamma_{12}$  where  $J_i = Q_i / h^2$  is the injection superficial velocity of fluid Li (i = 1, 2). While flow maps of fluid pairs E5h and E50 show similar arrangements of flow regions, differences in the relative areas and transitions between flow regimes are apparent. Overall, separated flows are observed at large  $Q_1$  and dispersed flows are found at small  $Q_1$ . In the droplet regimes, dripping flows with large wavelength  $\lambda$  are generated at low  $Q_2$  and jetting patterns with small  $\lambda$  occur at high  $Q_2$ . A somewhat similar behaviour is found for separated flows, where waves of large  $\lambda$  are observed at small  $Q_2$  and short waves are generated at large  $Q_2$ . Similar to our previous work on the development of interfacial waves in two-layer viscosity-stratified flows made of miscible or immiscible fluid pairs (Hu & Cubaud 2018), we classify the long wave regime as capillary waves and the short wave configuration as inertial waves. In the capillary wave regime, the wavelength  $\lambda$  increases along the flow direction before stabilizing, and the inertial regime is characterized with a spatially decreasing  $\lambda$ , which reaches a nearly constant value further downstream. An apparently stable core-annular flow regime is also found in the experimental field of view for intermediate values of  $Q_1$  at large  $Q_2$ . In addition, unsteady variations of basic droplet flow patterns are located near wave regime transitions due, in particular, to a small droplet spacing L leading to coalescence in the unsteady dripping and jetting regimes. Likewise, complex spatial variations of  $\lambda$  are observed in the unsteady wave regime between the capillary and inertial wave regimes, where the wavelength  $\lambda$  first decreases and then increases along the flow direction. Finally, a displacement regime, where the high-viscosity fluid L2 engulfs the low-viscosity fluid L1 channel resulting in no periodic pattern, is identified for very large  $Q_2$  and low  $Q_1$ . This limiting case is found below low flow rate ratios  $\varphi = Q_1/Q_2$ , such as  $1.25 \times 10^{-2}$  for fluid pair E5h and  $5 \times 10^{-3}$  for E50 as shown in figure 2 and presents analogies with the situation where the high-viscosity fluid is injected from the central channel of a square hydrodynamic focusing section (Cubaud & Mason 2008). Other transitional lines on the flow map are discussed in following sections. In particular, we derive analytical criteria to unravel basic flow features and elucidate the transition curve between dispersed and separated flows across all regimes.

### 4. Dispersed flows

Dispersed flow regimes comprise both steady and unsteady dripping and jetting flow patterns. The dripping regime is obtained at low capillary numbers for small flow rates  $Q_1$  and  $Q_2$  and is one of the most widely encountered regimes in microfluidic applications in the chemical and biological fields, where droplets are used as reaction chambers. By contrast, the jetting regime is reached at moderate capillary number and find use to generate small droplets with applications in drug delivery. In this context, predicting the size of the droplet d has received considerable attention in microfluidic studies (Anna 2016). Here, we systematically examine the morphology and dynamics of droplets flows based on droplet length d, spacing L, and velocity  $V_D$  for a wide range of flow rates and three different fluid pairs with a highly viscous continuous phase.

## 4.1. Droplet mobility

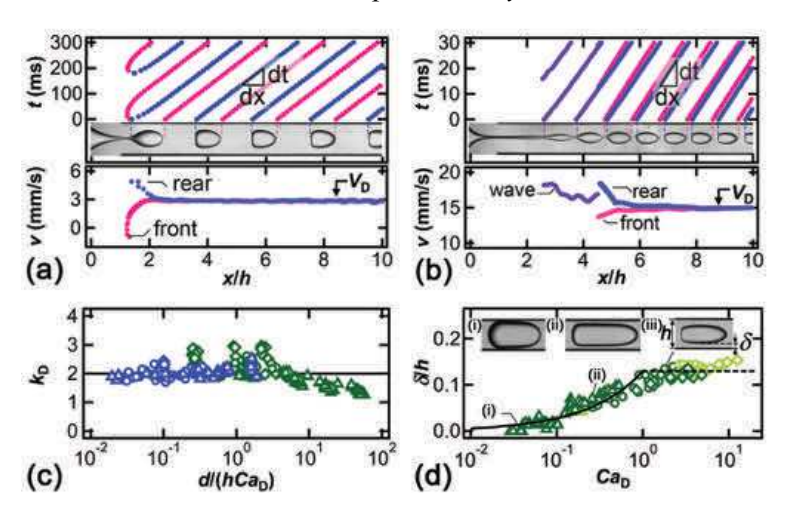


FIGURE 3. (Color online) Droplet velocity and normalized film thickness. Droplet velocity  $V_D$  is measured on the traces for (a) dripping  $[(Q_1, Q_2), \text{fluid pair}] = [(1, 4), E5h]$  (Flow rates in  $\mu$ L/min) and (b) jetting flows [(4, 20), E5h]. (c) Evolution of droplet mobility, solid line:  $k_D = 2$ .  $(E50(\triangle), E5h(O))$  and  $E5k(\diamondsuit)$ ). (d) Normalized film thickness  $\delta/h$  vs droplet capillary number Ca<sub>D</sub>. Solid line:  $\delta/h = 0.13 \text{ Ca}_D^{2/3}$  (Ca<sub>D</sub> < 1). Dashed line:  $\delta/h = 0.13 \text{ (Ca}_D > 1)$ . Inset: Micrographs of deformed droplets (i) [(0.5, 1), E50], (ii) [(5, 2), E50], and (iii) [(4, 4), E5h].

We first examine the velocity  $V_D$  of droplets in the dripping and jetting regimes. To measure  $V_D$ , spatial-temporal (x-t) diagrams are generated by tracking the front  $x_F$  and rear  $x_R$  positions of droplets using high-speed imaging. For steady dripping and jetting flows, the measured front and rear velocities,  $V_F = dx_F/dt$  and  $V_R = dx_R/dt$ , of all droplets form specific curves that merge further downstream to reach a constant value  $V_D$  (figure 3(a) and (b)). By contrast, for unsteady dripping and jetting flows, the spatial evolution of velocity slightly differs from droplets to droplets. For both steady and unsteady flows, the average droplet velocity  $V_D$  is compared to the multifluid flow superficial velocity  $J_T = (Q_1 + Q_2)/h^2$ , such as  $V_D = k_D J_T$ , where  $k_D$  is the droplet mobility coefficient. The coefficient of droplet mobility  $k_D$  typically decreases with the droplet length d and grows with the capillary

number of the continuous phase  $Ca_D = V_D \eta_2/\gamma_{12}$ , which controls the thickness of the lubricating layer  $\delta$  between droplets and walls. Measurements of  $k_D$  are reported as a function of  $d/(hCa_D)$  for all fluid pairs in steady dripping and jetting regimes in figure 3(c) and display an average value around  $k_D \approx 2$  in good agreement with the assumption that small droplets travel near the peak velocity of parabolic flows in square ducts,  $2.1J_T$ . Droplet mobility analysis typically includes droplet deformation, channel confinement and the presence of corner flows and lubricating films at the walls (Lac & Sherwood 2009; Jakiela, *et al.* 2011; Nath, *et al.* 2017; Rivero-Rodriguez & Scheid 2018). Here, measurements show that the mobility  $k_D$  is enhanced when d/h is small and  $Ca_D$  is large and data suggest the average droplet velocity scales as

$$V_{\rm D} = 2J_{\rm T}.\tag{1}$$

For confined droplets with length d > h, the relationship between film thickness  $\delta$  and capillary number Ca corresponds to the classic Bretherton problem (Bretherton 1961). In our square microchannels, the normalized film thickness follows the classic scaling such as  $\delta h = 0.13 \text{Ca}_D^{2/3}$  for moderate  $\text{Ca}_D < 1$  (figure 3(d)). For larger  $\text{Ca}_D$ , the film thickness reaches a plateau  $\delta h \approx 0.13$  similar to the case of water droplets in silicone oils with significantly larger  $\gamma_{12}$  (Jose & Cubaud 2014). The magnitude of the prefactor in the relationship between  $\delta$  and  $\text{Ca}_D$  depends on flow configurations and confinement geometry (Wong, Radke & Morris 1995; Balestra, Zhu & Gallaire 2018). Overall, the mobility coefficient has influence on flow morphology, in particular for the wavelength  $\lambda$  of segmented flows.

#### 4.2 Dripping

We now turn our attention to the morphology of dripping flows based on droplet length d and spacing L. In particular, we wish to predict the transition to separated flows when  $L \to 0$  based on fluid and flow parameters. Similar to the case of bubbles, where the internal viscosity is neglected, the droplet length is estimated as  $d = V_D T_2$ , where  $T_2$  is the pinching time corresponding to the filling of the junction by liquid L2,  $T_2 = h^3/Q_2$ . Introducing the continuous phase liquid fraction  $\alpha_2 = Q_2/(Q_1+Q_2)$  yields a scaling such as  $d/h = k_D/\alpha_2$  for the droplet size at low capillary numbers. At large Ca, however, the influence of viscous forces become significant and for a given fluid pair, the droplet size also depends on absolute flow velocity. To measure the influence of Ca, we fix  $\alpha_2$ , and measure the droplet size d as a function of  $Ca_2 = \eta_2 J_2/\gamma_{12}$  to find a scaling of the form  $d/h \sim Ca_2^{-1/3}$  (figure 4). While the droplet length d scales with  $(\alpha_2 Ca_2^{1/3})^{-1}$ , systematic shifts in data points are observed based on viscosity ratio  $\chi$ , which suggests the existence of a correction factor  $N_d$  associated with previous scaling. Hence, we curvefit dimensionless droplet length d/h as a function of  $N(\alpha_2 Ca_2^{1/3})^{-1}$  for each fluid pair and find a weak dependence on viscosity ratio  $N = 0.17 \chi^{-1/5}$  (figure 4). Finally, the normalized droplet length for all fluid pairs is shown to scale as

$$d/h = a(\alpha_2 \operatorname{Ca}_2^{1/3} \chi^{1/5})^{-1}, \tag{2}$$

where the constant a = 0.17. As expected, unsteady dripping regime are found for large droplet length d, however, a criterion solely based on d is not sufficient to predict regime transition as steady and unsteady regimes are found in the same area (figure 4 (a)).

The spacing L between droplets can be estimated using a similar argument in conjunction with mass conservation of segmented flows over a unit cell of equivalent wavelength  $\lambda = d + L$  and period T, where droplet length  $d \sim Q_1 T/h^2$  and spacing  $L \sim Q_2 T/h^2$ , which leads to the scaling  $d/L \sim Q_1/Q_2 = \varphi$ . While a detailed discussion of the aspect ratio d/L is presented later, the relationship  $d/L \sim \varphi$  in turn yields  $L/h \sim (d/h)/\varphi \sim (\alpha_1 \text{Ca}_2^{1/3} \chi^{1/5})^{-1}$ , where  $\alpha_1 = Q_1/(Q_1 + Q_2)$  is the dispersed phase volume fraction. Similar exponents are found experimentally with  $L/h \sim \text{Ca}_2^{-1/3}$  for fixed  $\alpha_1$  and correction factor  $N_L = 0.1 \chi^{-1/5}$  for different fluid pairs. Overall, the normalized spacing experimentally follows

$$L/h = b(\alpha_1 \text{Ca}_2^{1/3} \chi^{1/5})^{-1}, \tag{3}$$

where b = 0.1 (figure 4(b)). Data points depart from previous scaling for spacing L/h < 1 and  $\alpha_1 \text{Ca}_2^{1/3} \chi^{1/5} > 0.1$  as the flow becomes concentrated and finally leads to unsteady dripping regime for L/h < 0.5.

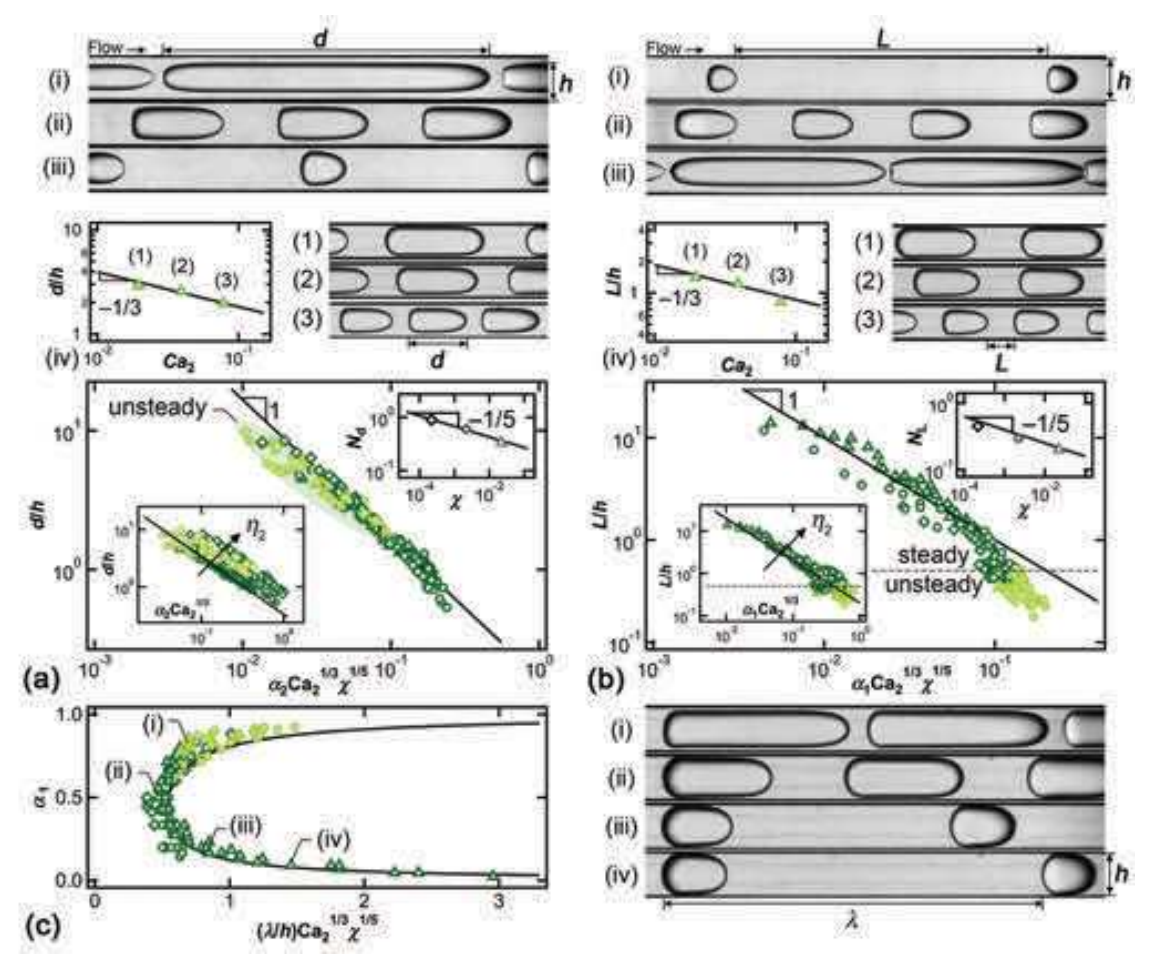


FIGURE 4. (Colour online) Dripping regime morphology with fluid pairs E50 ( $\triangle$ ), E5h ( $\bigcirc$ ) and E5k( $\diamondsuit$ ). (a) Main graph: Normalized droplet length d/h, solid line:  $d/h = 0.17(\alpha_2 \text{Ca}_2^{1/3} \chi^{1/5})^{-1}$ . Bottom inset: d/h vs.  $\alpha_2 \text{Ca}_2^{1/3}$ , solid line:  $d/h = 0.17(\alpha_2 \text{Ca}_2^{1/3} \chi^{1/5})^{-1}$ .

0.33( $\alpha_2 \text{Ca}_2^{1/3}$ )<sup>-1</sup>. Top inset: correction factor, solid line:  $N_d = 0.17\chi^{-1/5}$ . Micrographs (flow rates in  $\mu\text{L/min}$ ): (i)  $(Q_1, Q_2) = (10, 1)$ , (ii) (1, 1), and (iii) (0.1, 1). (iv) d/h vs Ca<sub>2</sub> for fixed  $\alpha_2 = 0.4$ , solid line:  $d/h = 0.85\text{Ca}_2^{-1/3}$ . Micrographs from (1) to (3):  $(Q_1, Q_2) = (1.5, 1)$ , (3, 2), and (6, 4). (b) Normalized droplet spacing L/h, solid line:  $L/h = 0.1(\alpha_1\text{Ca}_2^{1/3}\chi^{1/5})^{-1}$ . Bottom inset: L/h vs.  $\alpha_1\text{Ca}_2^{1/3}$ , solid line:  $L/h = 0.5(\alpha_1\text{Ca}_2^{1/3})^{-1}$ . Top inset: correction factor  $N_L = 0.1\chi^{-1/5}$  (solid line). Micrographs: (i)  $(Q_1, Q_2) = (0.1, 2)$ , (ii) (1, 2), and (iii) (10, 2). (iv) L/h vs Ca<sub>2</sub> for fixed  $\alpha_1 = 0.5$ , solid line:  $L/h = 0.4\text{Ca}_2^{-1/3}$ . Micrographs from (1) to (3):  $(Q_1, Q_2) = (1, 1)$ , (2, 2), and (4, 4). (c) Rescaled dimensionless wavelength  $(\lambda/h)\text{Ca}_2^{1/3}\chi^{1/5}$  evolving with  $\alpha_1$ , solid line:  $(\lambda/h)\text{Ca}_2^{1/3}\chi^{1/5} = 0.17(1-\alpha_1)^{-1} + 0.1\alpha_1^{-1}$ . Micrographs: (i)  $(Q_1, Q_2) = (5, 1)$ , (ii) (1, 1), (iii) (0.2, 1) and (iv) (0.1, 1).

The equivalent wavelength  $\lambda = d + L$  of dripping flows is therefore estimated according to  $\lambda/h \approx a(\alpha_2 \text{Ca}_2^{1/3} \chi^{1/5})^{-1}$  +  $b(\alpha_1 \text{Ca}_2^{1/3} \chi^{1/5})^{-1}$ , which can be rewritten as  $(\lambda/h) \text{Ca}_2^{1/3} \chi^{1/5} \approx a \alpha_2^{-1} + b \alpha_1^{-1} = 0.17(1-\alpha_1)^{-1} + 0.1 \alpha_1^{-1}$ . When plot the rescaled dimensionless wavelength  $(\lambda/h) \text{Ca}_2^{1/3} \chi^{1/5}$  as a function of  $\alpha_1$ , data points for three fluid pairs collapse together and agree well with the derived formula (figure 4 (c)). The minimum  $\lambda$  is found at  $\alpha_1 = 0.5$  at the transition between diluted and concentrated droplets flows. As droplets are generated at the fluid junction in the dripping regime, our work shows that segmented are essentially dominated by the liquid fraction with small correcting factors based on capillary number and viscosity ratio. As the side flow rate  $Q_2$  increases, the capillary breakup instability becomes convected further downstream in the jetting regime.

### 4.3 Jetting

The jetting regime corresponds droplet formation through the breakup of an initially stable central stream at a distance  $L_S$  from the junction. Droplets are periodically emitted from the central stream, which we label primary flow, due to the development of Rayleigh-Plateau instabilities (figure 5(a)). In this section, we combine the periodicity and instability analysis to understand the dynamics and morphology of jetting flows

#### 4.3.1 Primary flow

The primary flow is modeled as a time-invariant core-annular flow without significant development of instability patterns near the fluid junction. Flow characteristics include the inner stream diameter  $\varepsilon$ , average velocities of both inner and outer streams,  $V_1$  and  $V_2$ , and interfacial velocity  $V_i$ , which depends on control parameters, including flow rates and fluid viscosities,  $Q_1$ ,  $Q_2$ ,  $\eta_1$  and  $\eta_2$ . We consider a simplified one-dimensional model of core-annular-flow in a circular channel, which provides a useful approximation to a compact square channel, especially when  $\varepsilon$  is small. Following the analysis of (Cao, *et al.* 2003) in the Stokes regime, the stream diameter  $\varepsilon$  is determined by the flow rate ratio  $\varphi$  and the viscosity ratio  $\chi$  according to

$$\frac{\varepsilon}{h} = \sqrt{\frac{1 + \varphi - \sqrt{1 + \varphi \chi^{-1}}}{2 + \varphi - \chi^{-1}}} \ . \tag{4}$$

The diameter  $\varepsilon$  allows for estimating average velocities according to  $V_1 = 4Q_1/(\pi \varepsilon^2)$  for the inner stream and  $V_2 = 4Q_2/(4h^2 - \pi \varepsilon^2)$  for the outer stream. As the inner stream diameter  $\varepsilon$  is seen to slightly increase along the flow direction due to entrance effects and instability development (figure 5(a)), the mean  $\varepsilon$  is measured in the middle of the stable stream at  $x = L_S/2$  and data show excellent agreement with Eq. (4), in particular, for low values of  $\varepsilon$  at different  $\chi$  (figure 5(b)). An asymptotic behaviour is found for low viscosity ratios  $\chi$  « 1 by simplifying Eq. (4) according to

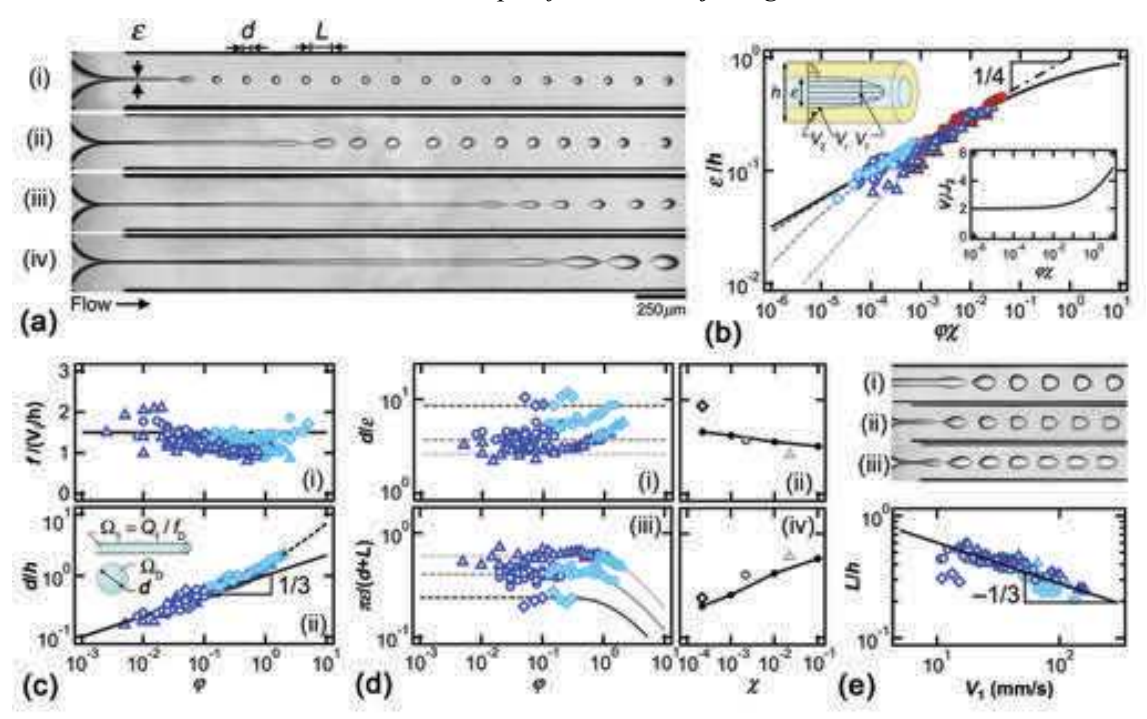
$$\varepsilon/h = (1 + (\varphi \chi)^{-1/2})^{-1/2},\tag{5}$$

which is a function of  $\varphi\chi$  only and agrees well with experimental data. Over our range of parameters, locally stable jets are observed for  $\varphi\chi$  « 1 when Eq. (4) further reduces into a scaling of the form  $\varepsilon/h \approx (\varphi\chi)^{1/4}$  (figure 5 (b)). This simple relationship provides insights into the dependence of  $V_1$  on  $Q_1$  and  $Q_2$  as  $V_1 \sim 4(Q_1Q_2)^{1/2}/(\pi h^2\chi^{1/2})$ , which is proportional to the geometrical mean of injection flow rates.

An important characteristic of separated flows is the interfacial velocity  $V_i$ . For a core-annular flows in a circular pipe, analytically solving Stokes equations yields  $V_i = 2V_2$ , where  $V_2 = 4Q_2/(4h^2 - \pi \varepsilon^2)$  is the average velocity of the outer stream. For square channels, we approximate  $V_i$  using Eq. (5) and obtain

$$V_{\rm i} = 2[1 + (4/\pi - 1 + 4/\pi(\varphi \chi)^{-1/2})^{-1}]J_2, \tag{6}$$

where  $J_2 = Q_2/h^2$ . This expression is found to overlap with the exact solution of Eq. (4) and clearly shows that the approximation  $V_i/J_2 \approx 2$  is valid for  $\varphi \chi < 0.1$  (figure 5(b) bottom inset).



4.3.2. Droplet formation in jetting

FIGURE 5. (Colour online) Jetting regime with fluid pairs E50 ( $\triangle$ ), E5h ( $\bigcirc$ ) and E5k( $\bigcirc$ ). (a) Micrographs of jetting streams (flow rates in  $\mu$ L/min): (i) ( $Q_1$ ,  $Q_2$ ) = (0.1, 10), (ii) (0.5, 20), (iii) (1, 40), and (iv) (2, 40) (fluids E5h). (b) Inner stream size  $\varepsilon h$  as a function of  $\varphi \chi$ . Solid line:  $\varepsilon h = (1+(\varphi \chi)^{-1/2})^{-1/2}$ , dot dashed line:  $\varepsilon / h = (\varphi \chi)^{1/4}$ , dashed lines: Eq. (4). Top inset: schematics of velocity profile in a core-annular flow. Bottom inset:  $V_i/J_2$  as a function of  $\varphi \chi$ . Solid line: Eq. (6). (c) Influence of  $\varphi$ . (i) Droplet emission frequency f, solid line:  $fh/V_i = 1.5$ . (ii) Normalized droplet length d/h, solid line:  $d/h = \varphi^{1/3}$ , dashed line:  $d/h = \varphi^{1/3} + \varphi/2$ . (d) Comparison with linear instability analysis. (i)  $d/\varepsilon$  as a function of  $\varphi$  for various  $\chi$ . (ii) average  $d/\varepsilon$  vs.  $\chi$ . Solid line: Tomotika's theory. (iii) Mode of maximum instability  $\pi \varepsilon / (d+L)$  versus  $\varphi$ . Average mode as a function of  $\chi$ . Solid line: Tomotika's theory. (e) L/h vs  $V_1$ , solid line:  $L/h = 1.3V_1^{-1/3}$ . Micrographs for fixed  $\varphi = 0.1$ , (i) [(2, 20), E50], (ii) [(1, 10), E5h], and (iii) [(0.2, 2), E5k].

Similar to a wave phenomenon, the periodic droplet emission pattern in the jetting regime is characterized by a frequency f, droplet velocity  $V_D$ , and wavelength  $\lambda = V_D/f$ . As droplets are generated through the break-up of the inner stream due to growing disturbances propagating along the flow direction, the droplet emission frequency f is expected to scale as the interfacial wave frequency before break-up. Previous work on the development of capillary and inertial waves of viscosity-stratified flows (Hu & Cubaud 2018) showed direct proportionality between wave frequency f and characteristic shear rate, such as  $f \sim V_i/h$ . Here, we normalize f with  $V_i/h$  and probe the influence of the flow rate ratio  $\phi$  on the droplet emission (figure 5 (c)(i)). For all fluid pairs, the normalized droplet emission frequency in the jetting regime remains more or less constant according to

$$fh/V_i \approx 1.5.$$
 (7)

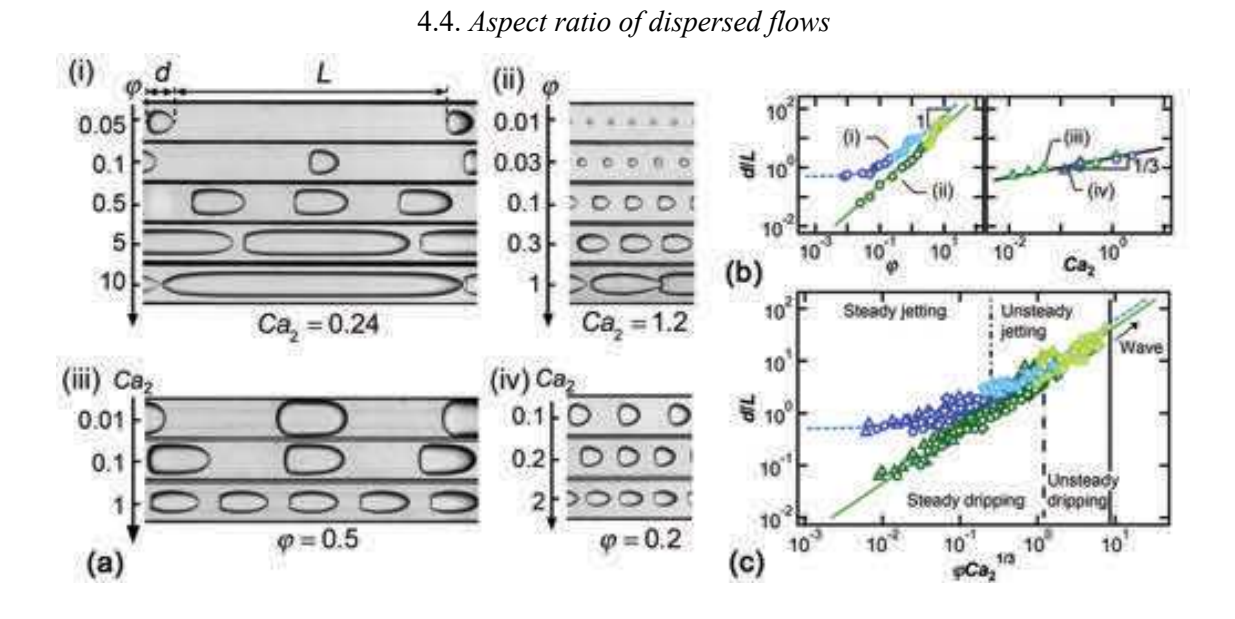
Information about droplet frequency f and jet diameter  $\varepsilon$  in turn allows for estimating the final droplet length d using mass conservation before and after the inner stream breakup. Balancing the equivalent droplet volume of the inner stream  $\Omega_1 = Q_1/f$  with a spherical droplet approximation  $\Omega_D = \pi d^3/6$  yields normalized droplet length d/h  $\approx [4J_1/(\pi V_i)]^{1/3} = \{3/4 \varphi [1+(\varphi \chi)^{-1/2}]^{-1}\}^{1/3}$ , which is a function of flow rate ratio  $\varphi$  and viscosity ratio  $\chi$  and can be simplified as

$$d/h \approx \varphi^{1/3} \tag{8}$$

when  $\varphi \chi \ll 1$ . Figure 5(c)(ii) shows good agreement with experimental data for small droplets, d/h < 1. A departure from the scaling relationship is observed for larger droplets d/h > 1, which are typically found in the unsteady jetting regime (figure 5 (a) (iv)). Droplets in this case become significantly deformed due to wall confinement and large capillary numbers. Overall, all data points are well fit with an expression of the form  $d/h = \varphi^{1/3} + \varphi/2$ .

Therefore, for very small viscosity ratio  $\chi \ll 1$ , the droplet length d in the jetting regime does not depend on inner nor outer fluid viscosities. To better understand this result, we investigate the relationship between droplet size d and jet diameter  $\varepsilon$  in the light of Tomotika's theory of Rayleigh-Plateau instability for an initially circular thread in a quiescent fluid (Tomotika 1935). In particular, in the steady jetting regime, the quantity  $d/\varepsilon$  is found to remain fixed around a mean value that depends on the viscosity ratio  $\chi$  (figure 5(d)(i)). To compare our result

with linear stability analysis, we use the reported modes of maximum instability  $x_T = k\varepsilon_T/2$  as a function of  $\chi$ , where  $k = 2\pi/\lambda_T$  and  $\lambda_T$  is the most unstable wavelength. Considering mass conservation between jet varicose of wavelength  $\lambda_T$  and resulting droplet of diameter  $d_T$ ,  $\lambda_T \pi \varepsilon^2 / 4 = \pi d_T^3 / 6$ , together with  $\lambda_T = \pi \varepsilon_T / x_T$  allows us to derive the expected  $d_T/\varepsilon_T = [3\pi/(2x_T)]^{1/3}$ , which is a constant for each fluid pair and is compared with experimental data in figure 5(d)(ii). Deviation is observed for the fluid pair E5k as droplets are significantly elongated along the flow direction due to the large Ca of the outer fluid. To circumvent the limitations associated with droplet deformation, we measure the dispersed flow wavelength  $\lambda = d + L$  in figure 5(d)(iii) to directly compare experimental x  $=\pi\varepsilon/\lambda$  and theoretical  $x_T$  for each fluid pair (figure. 5(d)(iv)) and find the agreement fairly satisfactory. It is a remarkable property of jetting regime that the dimensionless droplet length  $d/h \sim \varphi^{1/3}$  at very small viscosity ratio  $\chi$  « 1 does not depend on  $\chi$  due to the balance of the jet diameter  $\varepsilon$  and the mode of maximum instability of confined microjets. A somewhat equivalent property  $d/h \sim \varphi^{1/2}$  was also observed for the counterpart situation where viscosity ratio  $\chi$ » 1, albeit this behaviour was interpreted as a saturation of the mode of maximum instability due to a thread diameter  $\varepsilon$  being independent of  $\chi$  (Cubaud & Mason 2008). Here, the experimental  $\pi\varepsilon/\lambda$  is also found to remain stable in both steady and unsteady jetting regimes as droplet length d and spacing L compensate one another to match the theoretical wavelength  $\lambda_T$ . This observation highlights the importance of the viscosity ratio in the thread breakup process compared to external flow configurations. Here, we find that droplets in the jetting regime are always densely arranged with fine variations of L/h < 1. Experimental data show a relationship between droplet spacing L and the inner stream average velocity  $V_1$  according to  $L/h \sim V_1^{-1/3}$  (figure 5(e)) suggesting that a faster inner stream leads to a shorter distance between droplets, which eventually leads to the formation of a continuous stream in the separated flow region.



13

FIGURE 6. (Colour online) Aspect ratio of dripping and jetting regimes for fluid pairs E50 ( $\triangle$ ), E5h ( $\bigcirc$ ) and  $E5k(\diamondsuit)$ . (a) Micrographs of dispersed flows with various d/L for (i) dripping with  $Ca_2 = 0.24$ , (ii) jetting for  $Ca_2 = 1.2$ , (iii) dripping with  $\varphi = 0.5$  and (iv) jetting with  $\varphi = 0.2$ . (b) Influence of  $\varphi$  and  $Ca_2$  on aspect ratio d/L for cases shown in (a). (c) Evolution of d/L as functions of  $\varphi Ca_2^{1/3}$  for all cases. Solid line:  $d/L = 4.5 \varphi Ca_2^{1/3}$ . Dashed line:  $d/L = 0.5 + 4.5 \varphi Ca_2^{1/3}$ .

While dripping and jetting flows display specific behaviours, both regimes transition to separated flows when  $L \to 0$  and the linear aspect ratio d/L provides a useful method to characterize a wide range of segmented flows (figure 6(a)). Using continuity applied to a one-dimensional model of a repetitive unit of dispersed flows of length  $\lambda$  over a period T, such as  $dh^2 \sim Q_1T$  and  $Lh^2 \sim Q_2T$ , yields the simple relationship  $d/L \sim \varphi$ , which accurately represents the behaviour of dripping flows as well as jetting flows when d > h (figure 6(b)(i)). However, similar to our previous discussion of d/h and L/h, while flow rate ratio  $\varphi$  captures the major role of the relative flow rates (figures 6(a)(i, ii)), absolute flow rates also play a minor role in the morphology of dispersed flows as shown in figure 6(a)(iii, iv) with a visualization of flow patterns having similar  $\varphi$  but various Ca<sub>2</sub>. To capture the influence of Ca<sub>2</sub>, we plot the aspect ratio d/L as a function of Ca<sub>2</sub> for experiments having same flow rate ratio  $\varphi$  and find a relationship of the form  $d/L \sim \text{Ca}_2^{1/3}$  (figure 6(b)(ii)). Finally, the parameter  $\varphi$ Ca<sub>2</sub><sup>1/3</sup> permits rescaling of dripping flows according to

$$(d/L)_{\text{dripping}} = 4.5 \varphi \text{Ca}_2^{1/3}. \tag{9}$$

In contrast to the dripping regime where d/L can be as small as  $10^{-1}$ , the ratio d/L in jetting regime saturates at a constant value of around 0.5 for  $\varphi \operatorname{Ca}_2^{1/3} \ll 1$ . This behaviour is expected since  $d/L = d/(\lambda - d)$  and both  $d/\varepsilon$  and  $\lambda/\varepsilon$  are fixed for each fluid pair. Overall, d/L in jetting regime can be represented with the following formula

$$(d/L)_{\text{jetting}} = 0.5 + 4.5 \varphi \text{Ca}_2^{1/3}. \tag{10}$$

For relatively large flow rate ratio  $\varphi$ , jetting data points align with the dripping curve, suggesting similar flow morphology despite widely different droplet generation mechanisms (figure 6(c)).

The parameter  $\varphi Ca_2^{1/3}$  can also serves as an estimation of the transition from steady to unsteady dripping and jetting regimes as well as to wave regimes as indicated with dashed lines on figure 2. The critical value of  $\varphi Ca_2^{1/3}$  for flow transition slightly vary for each fluid pair whilst it remains on the same order of magnitude. A universal criterion for the transition between dispersed and separated flows, however, is still missing as the condition (d/L)  $\to \infty$  is not sufficient to predict flow regimes. In the following section, we examine the peculiar behaviour of separated flows and wave regimes and we develop an original method to delineate multiphase flow patterns in microchannels.

#### 5. Separated flows

#### 5.1. Capillary and inertial waves

Separated flow regimes consist of stable and wavy core-annular flows with a rich collection of flow morphologies. Two main types of waves are identified, including (i) inertial waves, whose wavelengths  $\lambda$  reach a maximum value near the fluid junction and then decrease along the flow direction and (ii) capillary waves, where  $\lambda$  monotonically increases along flow direction and saturates at a relatively large value further downstream (figure 7(a)). The characteristic wavelength  $\lambda/h$  of each experiment is measured at the plateau region downstream at around  $x/h \sim 10$  for both types of waves. Increasing the inner stream Reynolds number Re<sub>1</sub> =  $\rho_1 V_1 h/\eta_1$  allows us to examine the crossover between wave regimes with  $\lambda/h$  ranging from 1 to 10 (figure 7(b)).

Another important parameter is the wave emission frequency f, which is measured from spatiotemporal diagrams with f = 1/T, where T is the wave time period that is averaged over multiple cycles T = t/n (figure 7 (c)). Similar to our previous work on two-layer viscous stratifications (Hu & Cubaud 2018), the wave frequency f is related to the interfacial velocity  $V_i$  of the primary flow, i.e., stable core-annular flow, and direct proportionality between f and  $V_i$  is recovered for both capillary and inertial waves such as

$$f = 1.5V_{i}/h. (11)$$

This relationship is identical to that of the jetting regime for the droplet emission frequency and provides insights into the connection between wave and droplet flows.

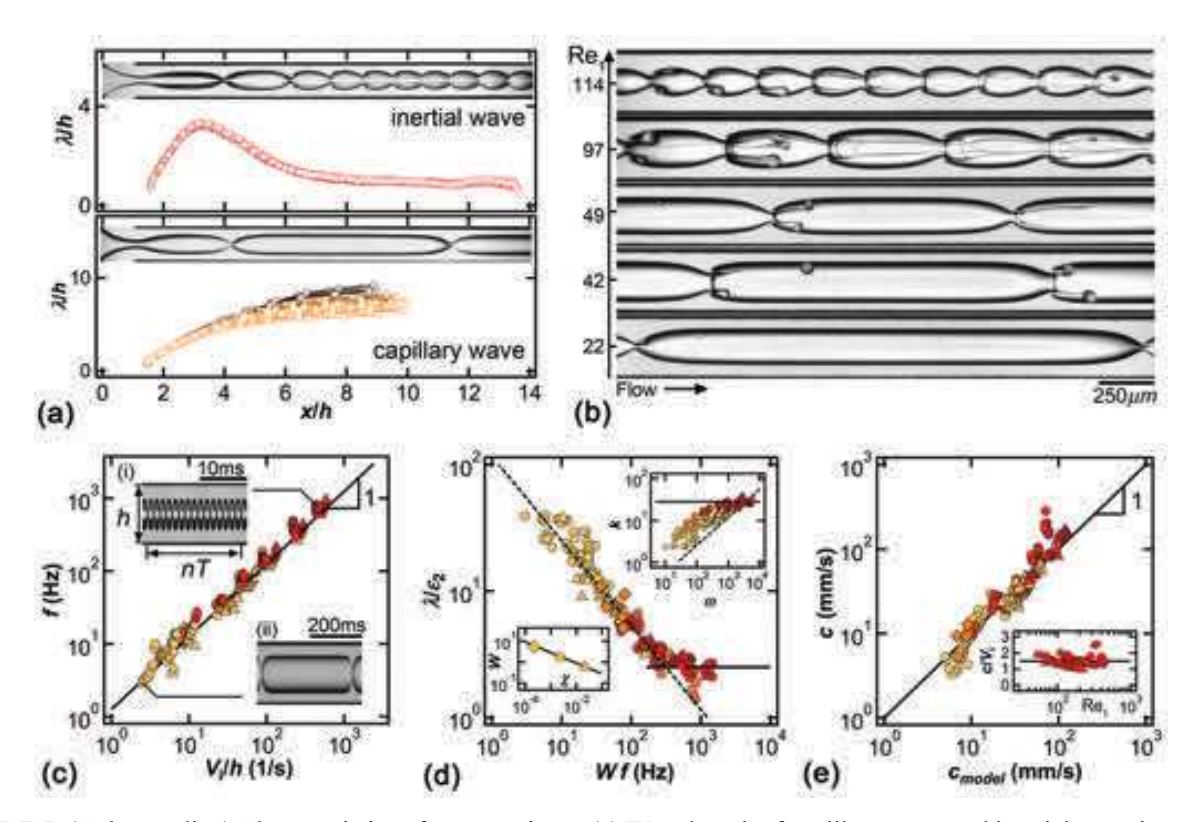


FIGURE 7. (Colour online) Characteristics of wave regimes. (a) Wavelength of capillary wave and inertial wave is measured at relatively downstream. (b) Evolution from capillary wave to inertial wave as Re<sub>1</sub> increases. (c) Wave emission frequency

 $f = 1.5V_i/h$ . Insets: spatiotemporal diagrams. (d) Evolution of wave aspect ratio  $\lambda/\epsilon_2$  as a function of Wf. solid line:  $\lambda/\epsilon_2 = 2.5$ . Top inset: capillary wave dispersion relationship  $k = [(\rho_1 + \rho_2)/\gamma_{12}]^{1/3} \omega^{2/3}$  (dashed line),  $k = 20 \text{ mm}^{-1}$  (solid line). Bottom inset: viscosity ratio coefficient  $W = 0.085 \chi^{-1/2}$  (solid line) (e) Wave celerity calculated according to equation (14) agrees well with experimental results. Bottom inset: inertial waves show  $c/V_i = 1.5$  over a wide range of Re<sub>1</sub>.

A common approach to study the time-space correlation of propagating waves is to examine the dispersion relationship such as  $D(k, \omega) = 0$ , where  $k = 2\pi/\lambda$  is the wavenumber that measures the wave spatial extension and  $\omega = 2\pi/1$  is the angular frequency that characterizes temporal periodicity. Therefore, we investigate the dispersion relationship of confined capillary waves in viscous liquid/liquid systems by plotting wavenumber k as a function of angular frequency  $\omega$  for all three fluid pairs. In general, data points follow the typical dispersion relationship derived for capillary waves propagating at a flat interface such as  $k = [(\rho_1 + \rho_2)/\gamma_{12}]^{1/3} \omega^{2/3}$  (figure 7(d) top inset), with good agreement for the coefficient  $[(\rho_1 + \rho_2)/\gamma_{12}]^{1/3} \approx 0.12 \text{ mm}^{-1}\text{s}^{2/3}$  and the exponent 2/3 associated with  $\omega$ . As we suspect data scattering due to various viscosity ratios  $\chi$  and interfacial curvatures  $2/\varepsilon$ , we rewrite the dispersion relationship as  $\lambda = [2\pi/\gamma_{12}/(\rho_1 + \rho_2)]^{1/3}f^{-2/3}$  using wavelength  $\lambda$  and frequency f directly and introduce the dimensionless viscous layer of thickness  $\varepsilon_2/h = (1-\varepsilon)/(2h)$  to consider the evolution of the dimensionless wavelength as  $\lambda/\varepsilon_2$ , by analogy with shallow water waves. We then plot  $\lambda/\varepsilon_2$  as a function of f and fit data according to  $\lambda/\varepsilon_2 = 2[2\pi/\gamma_{12}/(\rho_1 + \rho_2)]^{1/3}(Wf)^{-2/3}/h$ , where the coefficient  $W = 0.085\chi^{-1/2}$  depends on the viscosity ratio  $\chi$  (figure 7(d) bottom inset). Overall, experimental results collapse onto a single curve defined with a modified dispersion relationship that reads

$$\lambda/\varepsilon_2 = 2[2\pi\gamma_{12}/(\rho_1 + \rho_2)]^{1/3}(0.085\chi^{-1/2}f)^{-2/3}/h, \tag{12}$$

and can be approximated with  $\lambda/\varepsilon_2 \approx 10.4 h^{-1} [2\pi \chi \gamma_{12}/(\rho_1 + \rho_2)]^{1/3} f^{-2/3}$ . This relationship indicates the decrease of wavelength  $\lambda$  as the frequency f grows in the capillary regime. Eventually for large frequencies, the normalized wavelength  $\lambda/\varepsilon_2$  reaches the plateau associated with inertial waves according to

$$\lambda/\varepsilon_2 = 2.5. \tag{13}$$

The modified dispersion relationship is used to derive the wave propagation celerity  $c_{\text{model}}$  as a function of control parameters according to the basic wave equation  $c = \lambda f$  such as

$$c_{\text{model}} \approx 12 \left[ \frac{2\pi \chi \gamma_{12}}{(\rho_1 + \rho_2)h} \right]^{1/3} \frac{1 - \varepsilon^*}{(4 - \pi \varepsilon^{*2})^{1/3}} J_2^{1/3},$$
 (14)

where  $\varepsilon^* = \varepsilon/h$  is the dimensionless inner stream diameter. To measure the experimental wave celerity, we digitally track the motion of wave crests using image processing. The spatial evolution of c(x) is relatively similar to  $\lambda(x)$  and reaches a constant value in the observation channel. Overall, a good agreement is found between measured celerity c and  $c_{\text{model}}$  derived by equation (14) (figure 7 (e)). In addition, a simplified celerity model can also be

written for W = 1 as  $c_{\text{CAP}} = 2\{3\pi\gamma_{12}/[(\rho_1 + \rho_2)h]\}^{1/3}(1 - \varepsilon^*)(4 - \pi\varepsilon^{*2})^{-1/3}J_2^{1/3}$ . For inertial waves, we find that the celerity is comparable with interfacial velocity as  $c/V_i \approx 1.5$  over a wide range of Re<sub>1</sub> (figure 7(e) inset).

#### 5.2. Wave breaking

Interfacial viscous waves evolve and typically break with the entrainment of viscous filamentous structures from wave crests. While ligament formation and subsequent droplet generation is widely encountered in industrial and natural fragmentation processes, including spray formation (Marmottant & Villermaux 2004) and droplet splash (Wang & Bourouiba 2018), less is known about the extrusion of viscous filaments in confined microsystems. Here, we discuss two types of ligament formation, including rolling in the capillary regime and shearing in the inertial regime (figure 8). Both of these processes result from the large shear force exerted by the fast-inner stream on wave crests and the local wave structure that depends on wavelength  $\lambda$ .

The rolling ligament process (figure 8(a)(i)) is mainly observed for long waves with wavelength  $\lambda \gg h$  in the capillary regime and corresponds to the emission of a rolling tip which grows into a rotating droplet connected to the wave crest with a viscous thread. The rolling behaviour is induced by the viscous torque resulting from the parabolic velocity profile of the inner stream in the flow cells. As droplet migrate towards the wave trough, their velocity remains in slight excess of the wave celerity while the connected thread wraps around the droplet. Droplets eventually break from their "umbilical cords" supplying viscous material for growth through a complex thread thinning process. When the neck is narrow and a pair of ligaments are phase-locked, filaments can merge into a single ligament that travels near the centerline of the core-annular flow [figure 8 (a)(ii)]. Intriguing viscous bag formation mechanisms are also observed, where a rim of viscous material grows into a thin tubular shell. The viscous bag quickly destabilizes and interacts with ligaments and droplets further downstream [figure 8(a)(iii-iv)].

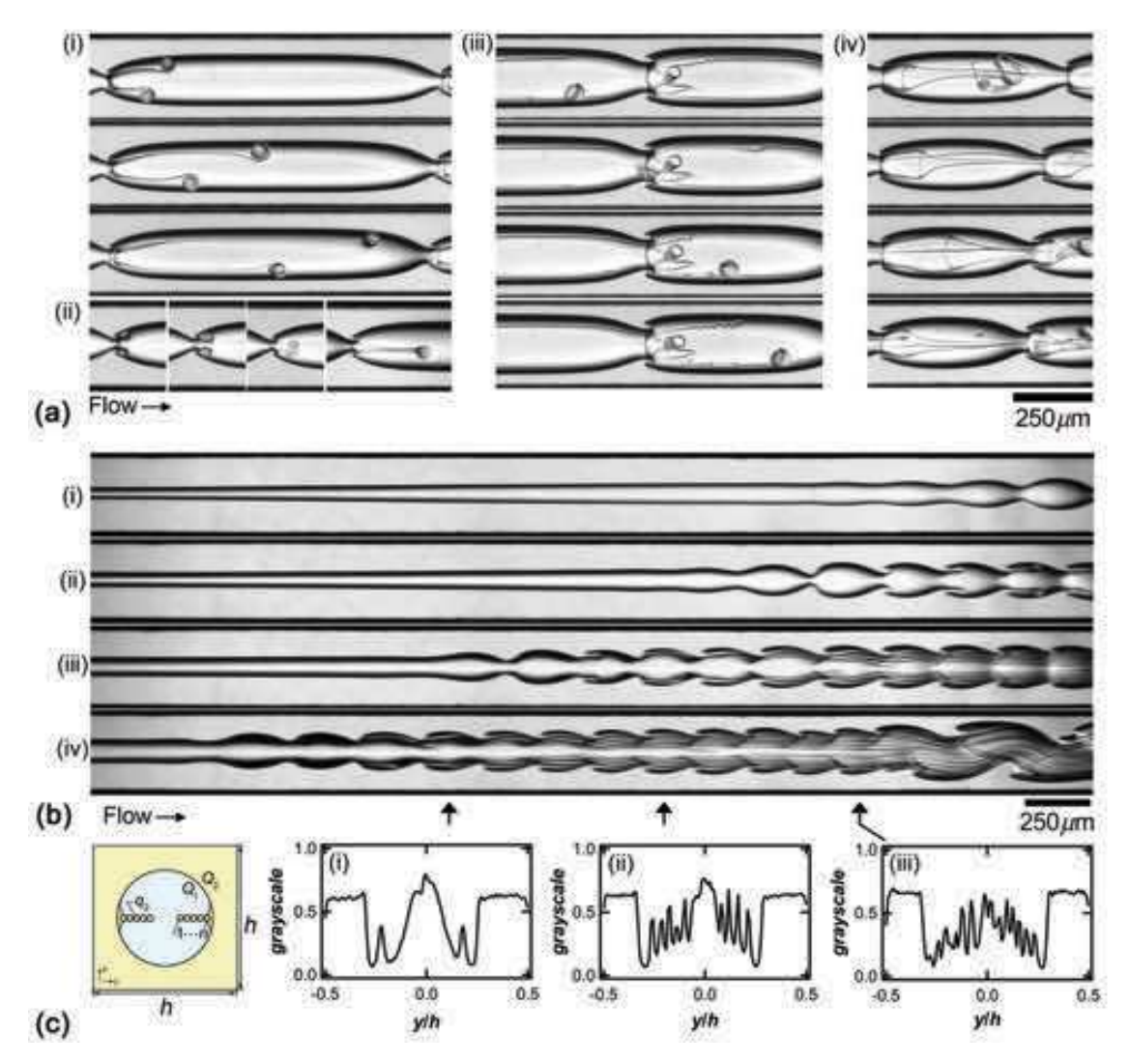


FIGURE 8. (Colour Online) Viscous ligaments due to wave breaking. (a) Formation process of ligaments with rolling tips. (i) A pair of ligaments  $[(Q_1, Q_2), \text{ fluid pair}, \Delta t] = [(100, 10), E5h, 10 \text{ ms}]$ . (ii) Merging ligaments [(70, 4), E5h, 14 ms], (iii) Viscous bag [(150, 20), E5h, 10 ms]. (iv) Transportation of detached viscous tip through a neck. [(250, 10), E5h, 1 ms] (b) Ligament threads. Flow rates of (i - iv) are  $Q_1 = 70, 150, 300, 600, \text{ and } Q_2 = 200, E50.$  (c) Schematic of ligament arrangement in cross-section view. (i - iii) Normalized gray-scale of cross flow direction, where local peaks represent ligaments.

In the inertial regime, the breaking of short waves with wavelength  $\lambda \sim h$  is characterized with the regular detachment of continuous streams of viscous material from the wave crest. In contrast with the capillary regime, filaments remain aligned with the wave crest due to the inertia associated with the fast- inner stream and the tip velocity is much larger than the wave celerity. In practice, multiple ligament formation is enhanced by increasing the inner stream flow rate as shown in figure 8 (b). An important quantity of high-viscosity fluid is convected through filament detachment resulting in the spatial depletion of the outer viscous layer with a progressive migration of wave crest toward the walls. This process produces the self-alignment of ligaments, where newborn ligaments are always located closer to the centerline. Three cross-section gray-scale profiles are included in figure 8

(c) at different locations to document the regular increase of the number of ligaments along flow direction. Such highly complex flow structure can also experience secondary destabilization processes with the coalescence of waves further downstream.

### 6. Comparison and transition

#### 6.1. Initial stable length

The evolution of the stable length  $L_{\rm S}$  of core-annular flows with flow rates provides useful information about flow regimes and transitions between dripping, jetting, wavy flow patterns. To measure the average length  $L_{\rm S}$  for a given set of control parameters, we superpose about 200 frames of a high-speed video to produce a composite image and visualize the average envelope of flow to measure the length of the invariant inner stream (figure 9(a)(i)). While the length  $L_{\rm S} \sim 0$  remains constant in the dripping regime,  $L_{\rm S}$  increases with flow velocity in the jetting regime and decreases with flow rates in the wave regimes.

To illustrate this behaviour, we plot normalized initial stable length  $L_S/h$  as a function of inner stream flow rate  $Q_1$  for fixed outer stream flow rate  $Q_2$  on figure 9(a)(i), which corresponds to the flow patterns shown on figure 9(b). The length  $L_S$  monotonically increases with  $Q_1$  in the jetting regime until no disturbance can be observed in the field of view, *i.e.*, for  $L_S/h > 16$ , which corresponds to the stable core-annular flow in this study. Further increase of  $Q_1$  leads to the wave regime, where  $L_S$  decreases with flow rates of injection. Such non-monotonic variation of  $L_S$  is also observed in open jets as flows evolve from dispersed to continuous regimes (Brennen 2005). To clarify the role of the inner stream diameter  $\varepsilon$  on the stable length  $L_S$ , a similar analysis is conducted on figure 9(a)(iii) for flows having a fixed  $\varphi$  but various absolute flow rates as shown in figure 9(c). In the dripping regime, the initial length  $L_S \sim 0$  at small flow rates, while for moderate flow rates,  $L_S$  sharply increases in the jetting regime, in particular above a critical value of outer stream capillary number  $Ca_2 \sim 0.5$ , which is in good agreement with previous studies in capillary tubes (Utada, *et al.* 2008).

The presence of a critical value  $Ca_2$  for the large growth of  $L_S$  suggests a distinction between slow flows, where  $L_S$  is independent of  $\varepsilon$  and follows a scaling of the total capillary number  $Ca_T$  as  $L_S/h \approx 3Ca_T^2$  (figure 9(d) bottom inset), and fast flows, where the stable length normalized with the jet circumference  $L_S/(\pi\varepsilon)$  depends on  $Ca_2$  according to  $L_S/(\pi\varepsilon) = 27Ca_2^{1/2}$  (figure 9(d) top inset), in the jetting regime and collapse on a master curve defined as  $L_S/(\pi\varepsilon) = 7/\varphi$  in the wave regimes (figure 9(d)). A similar behaviour was observed for the development on inertial waves in miscible viscous-stratified microflows (Hu & Cubaud 2016). In practice, we find that the initial stable length  $L_S$  growths with flow rates for convective instabilities and decreases with flow velocities for absolute instabilities. Further theoretical and numerical work would provide more insights on the dependency of  $L_S$  with control parameters. Better understanding the role of the stable length is important for hydrodynamic control of flow instabilities in microfluidic systems.

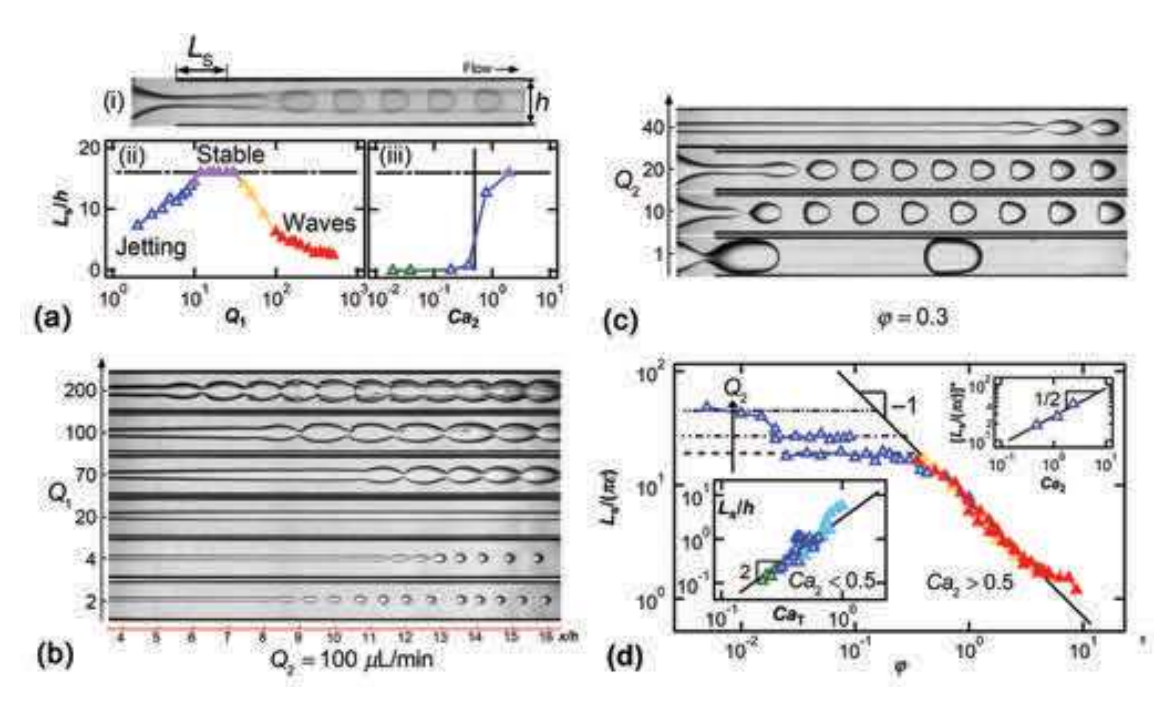


FIGURE 9. (Colour online) Initial length  $L_s$  for fluid pair E50. (a) (i)  $L_s$  is measured from image processing. (ii) Non-monotonic evolution of  $L_s/h$  is observed for fixed  $Q_2 = 100 \ \mu\text{L/min}$  and various  $Q_1$ . (b) Micrographs corresponding to (a). (c) Normalized  $L_s/h$  shows a sudden increase when  $Ca_2 > 0.5$  for fixed  $\varphi = 0.3$ . (d) Dimensionless initial length  $L_s/(\pi \varepsilon)$  for wave regime follows  $L_s/(\pi \varepsilon) = 7/\varphi$  (solid line), while jetting regime with  $Ca_2 > 0.5$  follows  $L_s/(\pi \varepsilon) = 27Ca_2^{1/2}$  as shown in top inset. Bottom inset: jetting regime for  $Ca_2 < 0.5$ ,  $L_s/h = 3Ca_1^2$  (solid line).

## 6.2. Periodicity of all regimes

In this section, we combine the periodic pattern description of dripping and jetting flows with capillary and inertial waves regimes. We discuss, in particular, the evolution of quantities such as pattern frequency f, wavelength  $\lambda$ , and velocity V across all flow regimes.

## 6.2.1. Temporal and spatial periodicity – frequency and wavelength

We first examine the pattern formation frequency f of dispersed and wave flows regimes. For given fluid pair, we present the evolution of the time period T = 1/f where each curve represents experiments conducted at fixed outer stream flow rate  $Q_2$  and varying inner steam flow rate  $Q_1$  (figure 10(a)(inset)). It is evident from this graph that (a) the inner stream flow rate  $Q_1$  does not significantly influence the period T of jetting and wave regimes but reduces the period T of dripping flows, and (b) the outer stream flow rate  $Q_2$  decreases the period for all regimes, suggesting that  $Q_2$  sets the level of T in general. These observations are consistent with our previous analysis of jetting and wave emission frequencies, where  $f \approx 1.5 V_i/h$  with  $V_i/h$  being largely determined by  $Q_2$ . Therefore, we use this reference and display the normalized frequency  $fh/V_1$  as a function of the injection capillary number  $Ca_{in} = J_1 \eta_2/\gamma_{12}$ , where  $J_1 = Q_1/h^2$ , for all fluid pairs across all regimes in figure 10 (a). As expected data for jetting and

wave regimes collapse on the curve  $fh/V_i = 1.5$ . In contrast, dripping regime features a smaller dimensionless frequency f that is curve-fitted with

$$fh/V_i = 1.5[1 + 0.25Ca_{in}^{-3/4}]^{-1},$$
 (15)

which reaches a plateau about 1.5 when  $Ca_{in} > 1$ . The upper limit of the dripping frequency is therefore given by  $f \approx 1.5 V_i/h$ , which is independent of interfacial tension but influenced by flow rates and fluid viscosities. Remarkably, the unsteady dripping and jetting regimes are observed in the same region when the two branches of steady dripping and jetting merges at the transition into wave regimes.

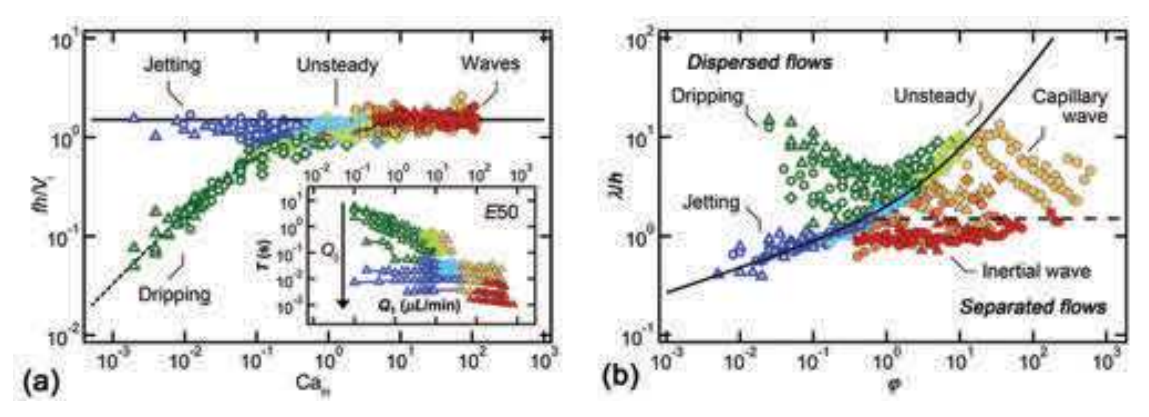


FIGURE 10. (Colour online) Frequency of dripping, jetting and wave regimes for fluid pairs E50 ( $\triangle$ ), E5h ( $\bigcirc$ ) and E5k( $\diamondsuit$ ). (a) Normalized frequency  $fh/V_i$  as a function of Ca<sub>in</sub>. Solid line:  $fh/V_i = 1.5$ . Dashed line:  $fh/V_i = 1.5(1+0.25\text{Ca}_{in}^{-3/4})^{-1}$ . Inset: evolution of T with  $Q_1$  as  $Q_2$  is varied, fluid pair E50 (b) Normalized wavelength  $\lambda/h$  as a function of  $\varphi$ . Solid line:  $\lambda/h = 1.5(\varphi^{1/4} + \varphi/3)$ , dashed-line:  $\lambda/h = 1.5$ .

The connection between dispersed and separated flows is also apparent when the periodic pattern wavelength  $\lambda$  is displayed as a function of the flow rate ratio  $\varphi$  (figure 10(b)). Regions of steady dripping and wave pattern data are clearly separated by a curve defined with the collapse of jetting and unsteady dripping data points. Hence, the jetting flow regime, which displays intermediate properties between separated and dispersed flows serves as the 'interface' between widely different flow regimes. The transitional curve can be inferred from the steady jetting regime for low  $\varphi$ . In this case, the wavenumber  $\pi e/\lambda$  remains constant for a given fluid pair, which yields the following scaling for dimensionless wavelength  $\lambda/h \sim e/h \sim \varphi^{1/4}$ . As the upper branch of the curve corresponds to unsteady dripping at large  $\varphi$ , the wavelength is then estimated as  $\lambda = V_D T$ , leading to  $\lambda/h = 2(J_1 + J_2)/(1.5V_i) \sim 1 + \varphi \sim \varphi$ . Combining both regimes,  $\lambda/h$  in jetting and unsteady dripping is fitted with  $\lambda/h = 1.5(\varphi^{1/4} + \varphi/3)$ . Overall, it is conceptually significant that the transition does not depend on fluid properties, such as interfacial tension and fluid viscosities when viscosity ratio  $\chi \ll 1$ , but only on flow rates  $Q_1$  and  $Q_2$ . A general criterion for the transition, however, is still missing as the intrinsic wavelength  $\lambda$  displays complex behaviour as a function of both fluid and flow properties.

### 6.2.2. Droplet/wave flow transition

To provide an overview of the evolution of the flow pattern features and probe the wave relationship  $\lambda = VT$  at the droplet/wave flow transition, we consider two type of crossovers, including (a) the dripping/capillary wave transition and (b) the jetting/inertial wave evolution as shown in figure 11. Since in general, the outer flow rate  $Q_2$  characterizes the magnitude of emission frequency f, we document flow evolution when the inner flow rate  $Q_1$  is varied and the outer flow rate  $Q_2$  is fixed, according to  $Q_2 = 2 \mu L/min$  to explore the dripping/capillary branch and  $Q_2 = 10 \mu L/min$  to examine the jetting/inertial wave transition. The change in period T and wavelength t0 is shown as a function of t2 for both cases in the panels (ii) to (iii) of figure 11 along with results of previous analysis, which are plotted in dashed lines for disperse flows and solid lines for separated flows for clarity.

For the dripping-capillary wave evolution, the non-monotonic variation of wavelength  $\lambda$  results from the initial decrease of period T with  $Q_1$  in the steady dripping regime until a minimal value is reached when the volume fraction of L1  $\alpha_1 = 0.5$  with  $Q_1 = 2 \mu L/min$ . Larger values of  $Q_1$  corresponds to the concentrated droplet regime and  $\lambda$  grows with  $Q_1$  until attaining the length of a capillary wave in the unsteady dripping (figure 11 (a)). Finally, the length of capillary waves decreases with  $Q_1$  as previously discussed. For the jetting-inertial wave evolution, the wavelength  $\lambda = V_D T$  monotonically increases with  $Q_1$  since  $V_D \sim J_1 + J_2$  and T saturates near a constant value for the jetting regime (figure 11(b)). When the wavelength of unsteady jetting grows to that of a capillary wave, streams separate and the flow progressively transitions from the capillary to inertial wave regime with a decrease of spatial period  $\lambda$ .

In contrast to the evolution of the spatial and temporal periods,  $\lambda$  and T, the behaviour of the periodic pattern velocity V is similar for both transitions and is characterized with a maximum velocity  $V_D = c$  at the crossover between dispersed and separated flows as seen on panels (iv) of figure 11. Indeed, the velocity of dispersed flows  $V_D$  scales with  $J_T$  that increases with  $Q_1$  and the celerity of waves c decreases with  $Q_1$ . Therefore, flow patterns adopt the branch having the smaller velocity between wave and droplet regimes, which minimizes dissipation. For example, the fast capillary waves propagating in the dripping and jetting regime are damped by the formation of relatively slow droplets further downstream (figure 3(b)). Once the equivalent droplet velocity  $V_D$  surpasses the wave celerity c, a wavy-core annular flow can form. The monotonic evolution of velocities in dispersed and separated flow regimes together with the simple identity  $V_D = c$  at the transition provides a useful criterion to predict flow regime selection.

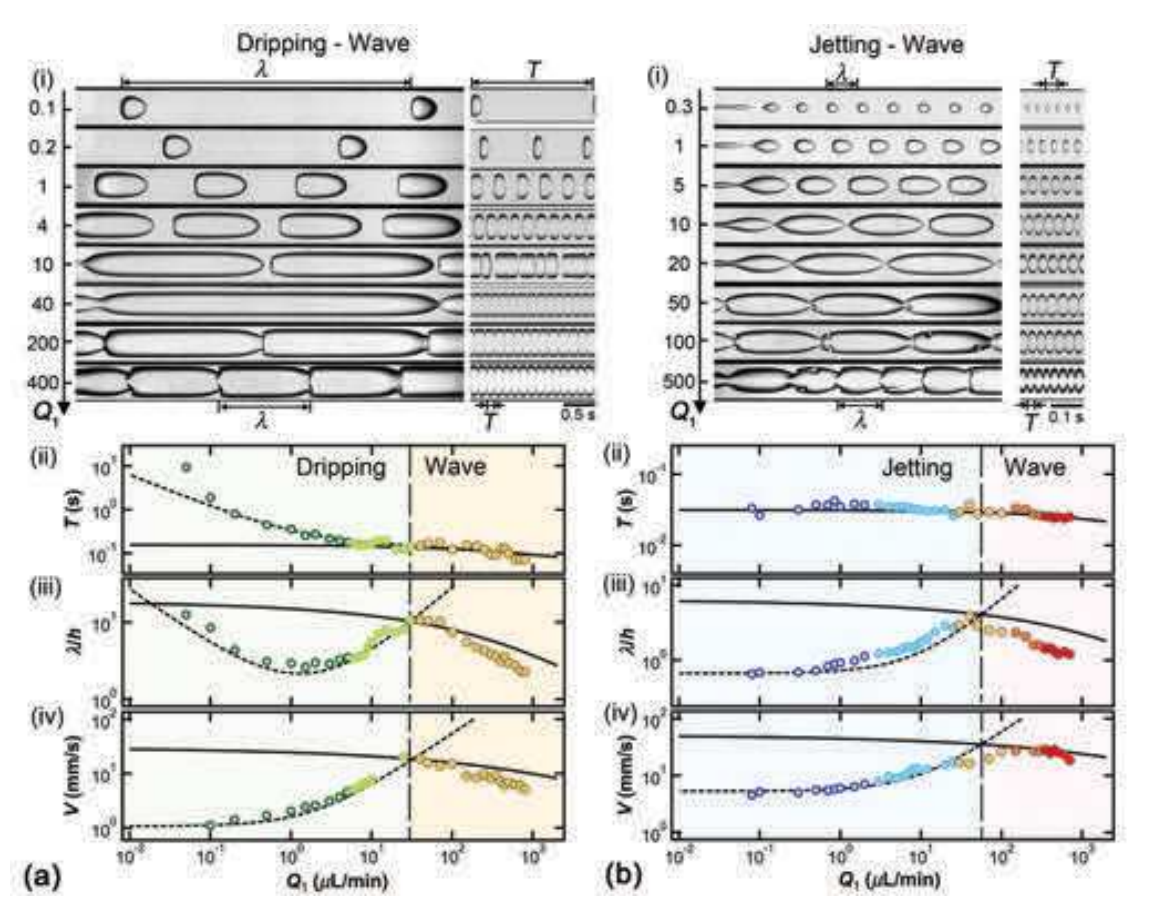


FIGURE 11. (Colour online) Evolution of pattern characteristics for dispersed to separated regimes, E5h (flow rates in  $\mu$ L/min). (a) Evolution from dripping to wave regime with fixed  $Q_2 = 2$ . (i) Micrographs and corresponding spatiotemporal diagrams at fixed  $Q_2$  for varying  $Q_1$ . Influence of  $Q_1$  on (ii) period T, (iii) wavelength  $\lambda/h$ , and propagation velocity V. Critical  $Q_1 = 30$  for dripping/wave transition. (b) Evolution from jetting to wave regime with fixed  $Q_2 = 10$ . Micrographs and corresponding spatiotemporal diagrams at fixed  $Q_2$  for varying  $Q_1$ . Influence of  $Q_1$  on (ii) period T, (iii) wavelength  $\lambda/h$ , and propagation velocity V. Critical  $Q_1 = 55$  for jetting/wave transition.

#### 6.3. Criterion for the transition from dispersed to separated flows

We now generalize the presence of a maximal velocity  $V_D = c$  at the transition between dispersed and separated flow regimes to develop a functional relationship to predict the critical flow rates for the transition. For any given flow rates and fluid viscosities  $(Q_1, Q_2, \eta_1, \eta_2)$ , velocities  $V_D$  and c can be expressed based on control parameters to develop an expression for the function

$$\beta = V_{\rm D}/c. \tag{16}$$

Assuming the wave adopts the typical capillary wave celerity  $c = c_{\text{CAP}}$  at the transition and the droplet velocity scales with the average flow velocity according to  $V_D = 2J_T$ , the critical flow rates at the transition when  $\beta = 1$  are expressed as a function of the flow rate ratio  $\varphi$  according to

$$Q_2^* = M(\rho, \gamma_{12}, h)F(\rho, \chi)h^2,$$
 (17)

and  $Q_1^* = \varphi Q_2^*$ . The function *M* is defined as

$$M(\rho, \gamma_{12}, h) = \left[\frac{3\pi\gamma_{12}}{(\rho_1 + \rho_2)h}\right]^{1/2}$$
 (18)

and corresponds to a characteristic capillary velocity based on fluid properties and confinement geometry, whose values for fluid pairs E50, E5h and E5k are 0.12 m/s, 0.15m/s and 0.16m/s. Therefore, the quantity  $Mh^2$  in Eq. (17) represents a characteristic flow rate modulated with the dimensionless function F, which is written as

$$F(\varphi,\chi) = \left[\frac{1-\varepsilon^*}{\left(4-\pi\varepsilon^{*2}\right)^{1/3}\left(1+\varphi\right)}\right]^{3/2}$$
(19)

and depends only on flow rate ratio  $\varphi$  and viscosity ratio  $\chi$ . This approach allows us to decorrelate the influence of viscous effects on the primary flow with F and the role of interfacial tension with M to examine the crossover between dispersed and separated flows. The method is employed to generate transition curves based on external control parameters and good agreement is found with experimental data as shown on figure 2.

We also use this technique to examine the expected influence of interfacial tension  $\gamma_{12}$  and viscosity ratio  $\chi$ on flow map transitional lines (figure 12). For a given set of densities and viscosities, the variation of  $\gamma_{12}$  modifies M as  $M \sim \gamma_{12}^{1/2}$  and an increase of the region associated with dispersed flow regimes is observed with increasing  $\gamma_{12}$  (figure. 12 (a)). In comparison, when all parameters remain fixed while the viscosity ratio  $\chi$  is manipulated, the transitional lines corresponding to the more viscous inner flow, i.e.,  $\eta_2/\eta_1 \ll 1$  reach an asymptotic curve for  $\eta_2/\eta_1 < 10^{-1}$  as the size of the highly viscous core becomes invariant to  $\chi$  in this situation. The calculated transitional curves are also in good agreement with previous experiments of a more viscous core (Cubaud & Mason 2008) and closely resembles the transition from dripping droplet flows to jets obtained through linear stability analysis of coaxial flows (Guillot, et al. 2007; Moiré, et al. 2017). In particular, the analogy in the results previously obtained through linear stability analysis for the dripping/wave transition, which takes place at low outer stream flow rate, and our criterion based on periodic pattern velocity is remarkable given the two distinct approaches employed and is promising for the development of a unifying framework to advance understanding of multiphase flows in confined microsystems. Over the large range of parameters investigated here, the plunging of the transition curve at large outer stream flow rate  $Q_2$  is also observed experimentally with the presence of the stable core-annular flows located in the separated flow region (figure. 12 (b)). Indeed,  $Q_2^* \sim Fh^2$  remains relatively constant at small  $\varphi$ , i.e., at large  $Q_2$  and small  $Q_1$  (figure. 12 (c)). While experiments were conducted for various viscosity contrasts  $\chi$  at relatively fixed interfacial tension  $\gamma_{12}$ , our analysis suggests the need for additional work on the influence of  $\gamma_{12}$  to refine predictive capabilities and further probe the effects of fluid properties and channel geometries on transitional curves.

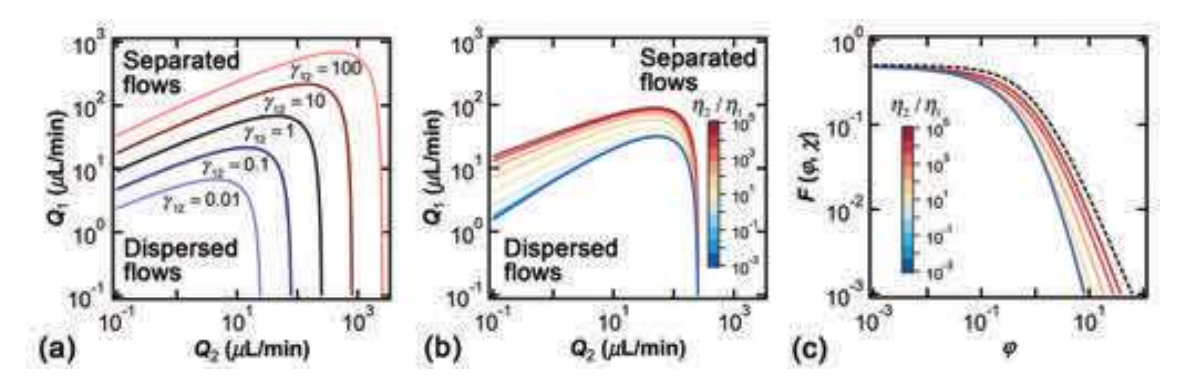


FIGURE 12. (Colour online) Parameter study of transition curves. (a) Influence of  $\gamma_{12}$  for  $\rho_1 = \rho_2 = 1$  g/mL,  $\eta_1 = 1$  cP,  $\eta_2 = 500$  cP, and  $h = 250 \mu \text{m}$  (b) Role of  $\chi$ . (c) Evolution of  $F(\varphi, \chi)$  versus  $\varphi$  for various  $\chi$ . Solid lines: Eq. (19), dashed line:  $F(\varphi, \chi) = 0.5(1+\varphi)^{-3/2}$ .

### 7. Conclusion

In this work, we present a comprehensive study of various dispersed and separated flow regimes using a single reference microgeometry. Immiscible viscosity-stratified flows with a thin core are produced over a large range of flow rates for various viscosity contrasts using a hydrodynamic focusing section. The use of fluids having low interfacial tension  $\gamma_{12}$  and different viscosities  $\chi \ll 1$  enables access to a wide range of flow phenomena to experimentally characterize hydrodynamic instabilities over vast flow maps. Over the range of parameters investigated, dispersed flows are observed for low inner stream flow rates  $Q_1$  with a dripping/jetting transition based on outer stream flow rate  $Q_2$  and separated flows are found at large  $Q_1$  with a capillary/inertial wave regime transition depending on  $Q_2$ . We systematically investigate the periodic pattern dynamics of droplet trains and interfacial waves with analysis of frequency f, celerity c and wavelength  $\lambda$ .

In the dripping regime, we show that droplet length d and spacing L primarily depend on volume fraction  $\alpha_1$  with minor corrections based on viscosity ratio  $\chi$  and capillary number  $Ca_2$  of side-flow. While the dripping wavelength  $\lambda = d + L$  reaches a minimum at half  $\alpha_1$ , separated flow transition occurs for large d and small L. In the jetting regime, the inner stream diameter  $\varepsilon$  of locally stable jets is well predicted analytically and the frequency of droplet emission f is directly proportional to the interfacial velocity or characteristic shear  $V_i/h$  of a stable core. We demonstrate that droplet length d depends on flow rate ratio according to  $\varphi^{1/3}$  and the jetting wavelength  $\lambda$  is in good agreement with classic theory of capillary breakup at various viscosity ratios  $\chi$ . Another important aspect is the evolution of the aspect ratio d/L, which quantifies the linear aspect ratio of droplet patterns and collapses all droplet data onto a single curve near the separated flow transition at large flow rate ratio  $\varphi$ .

For waves in the separated flow regime, we analyze the spatial evolution of wavelength  $\lambda$  and identify two regimes corresponding to long capillary waves and to small inertial wave patterns. In all cases, data indicate that

wave emission frequency is proportional to the interfacial velocity of the primary flow  $f \sim V_i/h$ , similar to the jetting regime and previous work on miscible viscous stratifications in microchannels. We then examine the dispersion relationship  $D(\lambda, f)$  of capillary waves in qualitative agreement with basic theory and show that the wave aspect ratio  $\lambda/\varepsilon_2$ , where  $\varepsilon_2$  is the thickness of the viscous layer, provides a useful parameter to account for the role of interfacial curvature and viscosity ratio on the development of capillary waves during separated flows in square microchannels. Following, the wave equation  $c = \lambda f$  is used to derive a functional relationship for the wave celerity as a function of control parameters. We finally discuss wave breaking phenomena, which lead to the formation of ligaments and viscous droplets and offer a novel route to continuously emulsify highly viscous materials in small geometries.

The unified description of dispersed and separated flows provides the means to better understand flow transitions. We discuss in particular the evolution of the stable length  $L_{\rm S}$  of base flow configurations with velocity in relation with the development of absolute and convective instabilities. Combining measurements of frequency f and wavelength  $\lambda$  across all regimes highlights the role of the capillary number and the flow rate ratio on pattern selection. In turn, this work shows that droplet velocity  $V_{\rm D}$  and wave celerity c meet at their highest value at the flow transition. A criterion based on periodic pattern velocity is then developed to predict the critical flow rates for transition in good accord with experimental data, which provides a complementary approach to linear stability analysis.

Overall, this study clarifies the role of fluid properties on the development of a wide range of microfluidic instabilities. Amongst various regimes of interest, the jetting regime display dual properties between dripping and waves regimes and the periodic flow velocity is shown to play a major role on pattern selection. Further theoretical and computational work would help better understand hydrodynamic flow transitions to improve design of microfluidic flow devices in a variety of situations. Here, the wave regime and wave breaking behaviour expand the scope of previously known microflow regimes and provide new opportunities for microfluidic applications.

### 9. Acknowledgements

This material is based upon work supported by the National Science Foundation under Grant No. CBET-1150389.

#### References

AL-WAHAIBI, T. & ANGELI, P. 2011 Experimental study on interfacial waves in stratified horizontal oil—water flow. *Int. J. Multiphase Flow* **37**, 930.

ANNA, S. L. 2016 Droplets and bubbles in microfluidic devices. Annu. Rev. Fluid Mech. 48, 285.

AUGELLO, L., FANI, A. & GALLAIRE, F. 2018 The influence of the entry region on the instability of a coflowing injector device. *J. Phys. Condens. Matter* **30**, 284003.

BALESTRA, G., ZHU, L. & GALLAIRE, F. 2018 Viscous Taylor droplets in axisymmetric and planar tubes: from Bretherton's theory to empirical models. *Microfluidics and Nanofluidics* **22**, 67.

BAROUD, C. N., GALLAIRE, F. & DANGLA, R. 2010 Dynamics of microfluidic droplets. Lab Chip 10, 2032.

BARRERO, A. & LOSCERTALES, I. G. 2007 Micro- and nanoparticles via capillary flows. Annu. Rev. Fluid Mech. 39, 89.

BERNA, C., ESCRIVÁ, A., MUNOZ-COBO, J. L. & HERRANZ, L. E. 2015 Review of droplet entrainment in annular flow: Characterization of the entrained droplets. *Progress in Nuclear Energy* **79**, 64.

BIRD, R. B., STEWART, W. E. & LIGHTFOOT, E. N., 2002 Transport phenomena (J. Wiley)

BRENNEN, C. E., 2005 Fundamentals of multiphase flow (Cambridge University Press)

BRETHERTON, F. P. 1961 The motion of long bubbles in tubes. J. Fluid Mech. 10, 166.

CAO, Q., VENTRESCA, A. L., SREENIVAS, K. R. & PRASAD, A. K. 2003 Instability due to viscosity stratification downstream of a centerline Injector. *Canadian J. Chem. Eng.* **81**, 913.

CHENG, L., RIBATSKI, G. & THOME, J. R. 2008 Two-phase flow patterns and flow-pattern maps: Fundamentals and applications. *App. Mech. Rev.* **61**, 0508021.

CROWE, C. T., 2006 Multiphase flow handbook (CRC Press)

CUBAUD, T. & MASON, T. G. 2008 Capillary threads and viscous droplets in square microchannels. *Phys. Fluids* 20, 053302.

CUBAUD, T. & NOTARO, S. 2014 Regimes of miscible fluid thread formation in microfluidic focusing sections. *Phys. Fluids* **26**, 122005.

CUBAUD, T., ULMANELLA, U. & HO, C.-M. 2006 Two-phase flow in microchannels with surface modifications. *Fluid Dyn. Res.* **38**, 772.

D'OLCE, M., MARTIN, J., RAKOTOMALALA, N., SALIN, D. & TALON, L. 2008 Pearl and mushroom instability patterns in two miscible fluids' core annular flows. *Phys. Fluids* **20**, 024104.

DRAZIN, P. G. & REID, W. H., 2004 Hydrodynamic stability (Cambridge University Press)

EGGERS, J. 1997 Nonlinear dynamics and breakup of free-surface flows. Rev. Mod. Phys. 69, 865.

EVANGELIO, A., CAMPOS-CORTÉS, F. & GORDILLO, J. M. 2016 Simple and double microemulsions via the capillary breakup of highly stretched liquid jets. *J. Fluid Mech.* **804**, 550.

GORDILLO, J. M., SEVILLA, A. & CAMPO-CORTÉS, M. 2014 Global stability of stretched jets: conditions for the generation of monodisperse micro-emulsions using coflows. *J. Fluid Mech.* **738**, 335.

GOVINDARAJAN, R. & SAHU, K. C. 2014 Instabilities in viscosity-stratified flow. Annu. Rev. Fluid Mech. 46, 331.

GUILLOT, P., COLIN, A., UTADA, A. S. & AJDARI, A. 2007 Stability of a jet in confined pressure-driven biphasic flows at low Reynolds numbers. *Phys. Rev. Lett.* **99**, 104502.

HINCH, E. J. 1984 A note on the mechanism of the instability at the interface between two shearing fluids. *J. Fluid Mech.* **144**, 463.

HU, X. & CUBAUD, T. 2016 Inertial destabilization of highly viscous microfluidic stratifications. *Phys. Rev. Fluids* 1, 044101.

HU, X. & CUBAUD, T. 2018 Viscous wave breaking and ligament formation in microfluidic systems. *Phys. Rev. Lett.* 121, 044502.

HUERRE, P. & ROSSI, M., 2005 Hydrodynamic instabilities in open flows. In Hydrodynamics and Nonlinear instabilities (Cambridge University Press)

JAKIELA, S., MAKULSKA, S., KORCZYK, P. M. & GARSTECKI, P. 2011 Speed of flow of individual droplets in microfluidic channels as a function of the capillary number, volume of droplets and contrast of viscosities. *Lab Chip* 11, 3603.

JOSE, B. M. & CUBAUD, T. 2014 Formation and dynamics of partially wetting droplets in square microchannels. *RSC Adv.* **4**, 14962.

JOSEPH, D. & RENARDY, Y., 1993 Fundamentals of two-fluid dynamics, Part II: Lubricated transport, drops and miscible liquids (Springer)

LAC, E. & SHERWOOD, J. D. 2009 Streaming potential generated by a drop moving along the centreline of a capillary. *J. Fluid Mech.* **640**, 55.

MARMOTTANT, P. & VILLERMAUX, E. 2004 On spray formation. J. Fluid Mech. 498, 73.

MOIRÉ, M., PEYSSON, Y., HERZHAFT, B., PANNACCI, N., GALLAIRE, F., AUGELLO, L., DALMAZZONE, C. & COLIN, A. 2017 Ultralow Interfacial Tension Measurement through Jetting/Dripping Transition. *Langmuir* 33, 2531.

MOWLAVI, S., SHUKLA, I., BRUN, P.-T. & GALLAIRE, F. 2019 Particle size selection in capillary instability of locally heated coaxial fiber. *Phys. Rev. Fluids* **4**, 064003.

NATH, B., BISWAS, G., DALAL, A. & SAHU, K. C. 2017 Migration of a droplet in a cylindrical tube in the creeping flow regime. *Phys. Rev. E* **95**, 033110.

NUNES, J. K., TSAI, S. S. H., WAN, J. & STONE, H. A. 2013 Dripping and jetting in microfluidic multiphase flows applied to particle and fibre synthesis. *J. Phys. D: Appl. Phys.* **46**, 114002.

RIVERO-RODRIGUEZ, J. & SCHEID, B. 2018 Bubble dynamics in microchannels: inertial and capillary migration forces. *J. Fluid Mech.* **842**, 215.

SALIN, D. & TALON, L. 2019 Revisiting the linear stability analysis and absolute-convective transition of two fluid core annular flow. *J. Fluid. Mech.* **865**, 743.

SANGALLI, M., GALLAGHER, C. T., LEIGHTON, D. T., CHANG, H. C. & MCCREADY, M. J. 1995 Finite-amplitude waves at the interface between fluids with different viscosity: Theory and experiments. *Phys. Rev. Lett.* **75**, 77.

SELVAM, B., MERK, S., GOVINDARAJAN, R. & MEIBURG, E. 2007 Stability of miscible core-annular flows with viscosity stratification. *J. Fluid. Mech.* **592**, 23.

TOMOTIKA, S. 1935 On the instability of a cylindrical thread of a viscous liquid surrounded by another viscous fluid. *Proc. Roy. Soc. A* **146**, 322.

TRIPLETT, K. A., GHIAASIAAN, S. M., ABDEL-KHALIK, S. I. & SADOWSKI, D. L. 1999 Gas-liquid two-phase flow in microchannels, Part I: two-phase flow patterns. *Int. J. Multiphase Flow* **25**, 377.

UTADA, A. S., FERNANDEZ-NIEVES, A., GORDILLO, J. M. & WEITZ, D. A. 2008 Absolute instability of a liquid jet in a coflowing stream. *Phys. Rev. Lett.* **100**, 014502.

WANG, Y. & BOUROUIBA, L. 2018 Unsteady sheet fragmentation: droplet sizes and speeds. J. Fluid Mech. 848, 946.

WONG, H., RADKE, C. J. & MORRIS, S. 1995 The motion of long bubbles in polygonal capillaries. Part 1. Thin films. *J. Fluid Mech.* **292**, 71.

YIH, C.-S. 1967 Instability due to viscosity stratification. J. Fluid Mech. 27, 337.